The history of ground ice formation and intra-permafrost fluid flow as documented by Ra and Th isotopes

Dotan Rotem[1], Yishai Weinstein[1], Yehudit Harlavan[3], Adi Torfstein[4,5], Hanne H. Christiansen[2]

[1]Department of Environment, Planning and Sustainability, Bar-Ilan University, Ramat-Gan, 529002, Israel.
[2]Department of Environmental Science, Aarhus University, Denmark.
[3]Geological Survey of Israel, 32 Yesha'yahu Leibowitz, Jerusalem 9692100, Israel.
[4]Institute of Earth Sciences, Hebrew University of Jerusalem, Jerusalem, Israel.
[5]The Interuniversity Institute for Marine Sciences, Eilat, Israel.

Corresponding to: Dotan Rotem dotanrotem1969@gmail.com

Abstract

While permafrost is considered a permanently frozen soil, it often demonstrates evidence for internal processes, including fluid migration. Here, we present data on the chemistry, Ra, Th, and Ac isotopes of saline permafrost from three closely retrieved cores drilled at Adventdalen, a fjord Valley in central Svalbard, which provides evidence for a fingering-style intra-permafrost recent fluid flow. Ground ice of the different cores differs markedly in its salinity and composition. In one core, which has a composition similar to seawater, the long to short-lived isotope activity ratios (AR), e.g., $(^{226}Ra/^{223}Ra)_{AR}$ and $(^{228}Ra/^{223}Ra)_{AR}$, are relatively low, being similar to parent isotope activity ratios ($^{230}Th/^{227}Ac$ and $^{230}Th/^{228}Th$, respectively) on grain surfaces (exchangeable fraction). Ground ice of another core, which is less saline and have Na/Cl and SO_4/Cl ratios higher than seawater, demonstrates much higher Ra isotope ratios, closer to parent ratios in the bulk sediment. Ground ice in a third core, with chemical composition similar to the latter, shows high $(^{226}Ra/^{223}Ra)_{AR,}$ albeit low $(^{228}Ra/^{223}Ra)_{AR.}$ It is suggested that the different isotope ratios are due to different residence times, and that the parameter controlling the longer-lived (^{226}Ra and ^{228}Ra) activities (hence, long to short isotope ratios) is radium diffusion from inside the grains via partly liquidized nano-pores. While ground ice in the less saline cores could have been formed during permafrost formation (10-9 ka), ground ice in the more saline core went recently (years to decades) through reset of its Ra clock, which did not allow a significant diffusion of the long-lived ^{226}Ra and ^{228}Ra from inside the grains. This reset is probably the result of a Late Holocene intrusion of saline fluids, which arrived from a low-Th or high water:rock ratio basement aquifer, and mixed with the original, less saline ground ice. Recent salinization is also supported by the presence of high salinity all the way up into the syngenetic permafrost, which has been deposited during the Late Holocene. The above highlights the internal dynamics of saline permafrost, which may affect its resilience to the ongoing global warming.

1. Introduction

Permafrost is a soil or rock that has remained at or below 0 °C for at least two consecutive years. While permafrost covers more than 20% of the northern hemisphere land area, it is evident that its distribution has dramatically declined during the last several decades, due to the ongoing global warming (Brown et al., 2002; Obu et al., 2019; Li et al., 2022), with continuous permafrost areas changing into discontinuous and sporadic permafrost zones (Kwong and Gan, 1994; Anisimov and Nelson, 1997; Osterkamp and Romanovsky, 1998; James et al., 2013).

While some of the permafrost is very old and thick, in particular in inland settings, such as Siberia, Canada, Alaska, and Antarctica (Gilichinsky and Wagener, 1995; Dobinski, 2011; Abramov et al., 2021), other areas are dominated by young permafrost (Late Pleistocene to Holocene), related to the last deglaciation, which exposed vast areas to the atmosphere and opened the way for cooling and permafrost formation (e.g., Jin et al., 2007; French, 2007). Following exposure, permafrost aggradation may go two ways. The first, applied to the already deposited sediments and bedrock, is the top-down, epigenetic permafrost formation, while the other is the bottom-up, syngenetic cooling and freezing of the newly deposited sediments.

Whereas most permafrost is significantly colder than 0°C, it is not necessarily strictly frozen (French, 2007; Dobinski, 2011; Keating et al., 2018), which is due to both the lowering of the freezing point in saline permafrost (Ahonen, 2001), as well as due to capillary or surface adsorption effects in the sediment pore space (e.g., Sheshukov and Nieber, 2011; Wang et al., 2020), which in turn could be related to water content and grain size (e.g., Zhang et al., 2018; Wang et al., 2021). The presence of fluids may boost intra-permafrost processes, allowing the re-distribution and migration of fluids in the cryotic pore space (Fisher et al., 2019; Lacelle et al., 2022).

Intra-permafrost processes are often associated with supra-permafrost processes, such as infiltration from the active layer (Mackay, 1983; Marsh and Woo, 1993; Boike et al., 1998), runoff on slopes to form foothill mounds (Åkerman and Malmström, 1986), intrusion from rivers (Alekseyev, 2015), and thaw-freeze crack-filling, which produce the commonly-observed ice wedges and polygon structures (e.g., Harry and Gozdzik, 1988; Mackay, 1989; Christiansen et al., 2005; Opel et al., 2018). On the other hand, intra-permafrost ice segregation is also common (Mackay, 1983; Mackay and Dallimore, 1992; Solomatin and Xu, 1994; Fu et al., 2022; Kipp et al., 2025). While this is more difficult to trace, Weinstein et al. (2019) showed by Ra and Th isotopes, combined with ^{3}H, that a segregated ice layer at Adventdalen, central Svalbard (Fig. 1), had been formed very recently (less than one year).

Naturally, due to its lower freezing temperature, saline permafrost (i.e., soils with significant content of soluble salts, such that results in a freezing point depression, e.g., Banin and Anderson, 1974; Marion, 1995) is more prone to fluid migration and intra-permafrost processes. Near-surface saline permafrost is widely distributed in the northern circumpolar region, especially in the continuous permafrost zone, covering up to 35% of that area (Brouchkov, 2002). The salinity source is commonly related to seawater (Hivon and Sego, 1993; Brigham-Grette and Hopkins, 1995; Forman et al., 2004; Lønne and Nemec, 2004; Jones et al., 2023), although it can also be strictly terrestrial, related to evaporation processes in inland basins and to water-rock interaction (e.g., Dickinson and Rosen, 2003; Henkemans, 2016; Gao et al., 2017). Salinity and cryotic state (i.e., freezing degree of the pore fluid) are highly heterogeneous in the saline permafrost environment (e.g., Brouchkov, 2002; Ahonen, 2001; Dafflon et al., 2016). This heterogeneity is sometimes manifested by the presence of lenses of unfrozen ground, or overcooled brines ('cryopegs'), which usually form due to freezing and salt expulsion processes (e.g., Yershov, 1998; Iwahana et al., 2021).

In Svalbard, near-surface saline permafrost is commonly observed in fjord valleys, where seawater ingression occurred during the early Holocene, following glacial retreat and sea level rise (e.g., Cable et al., 2018; Gilbert et al., 2019; Rotem et al., 2023). Permafrost formation had been inhibited until after seawater regression and the exposure of the recently deposited sediments to the atmosphere (Gilbert et al., 2018). The actual formation of the permafrost depends on the combination of climatic and soil physical attributes. Accordingly, while Hornum et al. (2020) argued that freezing at Adventdalen (Fig. 1) did not occur until 4500 years BP due to the relatively warm

mid-Holocene, Rotem et al. (2023) suggested that permafrost started forming immediately after exposure (ca. 9 ka), which was assisted by the thermal conductivity difference between solid ice and liquid water. In this paper, we show by chemistry and radioisotopes that the permafrost in eastern Adventdalen demonstrates a complex and multi-stage history of ground ice formation.

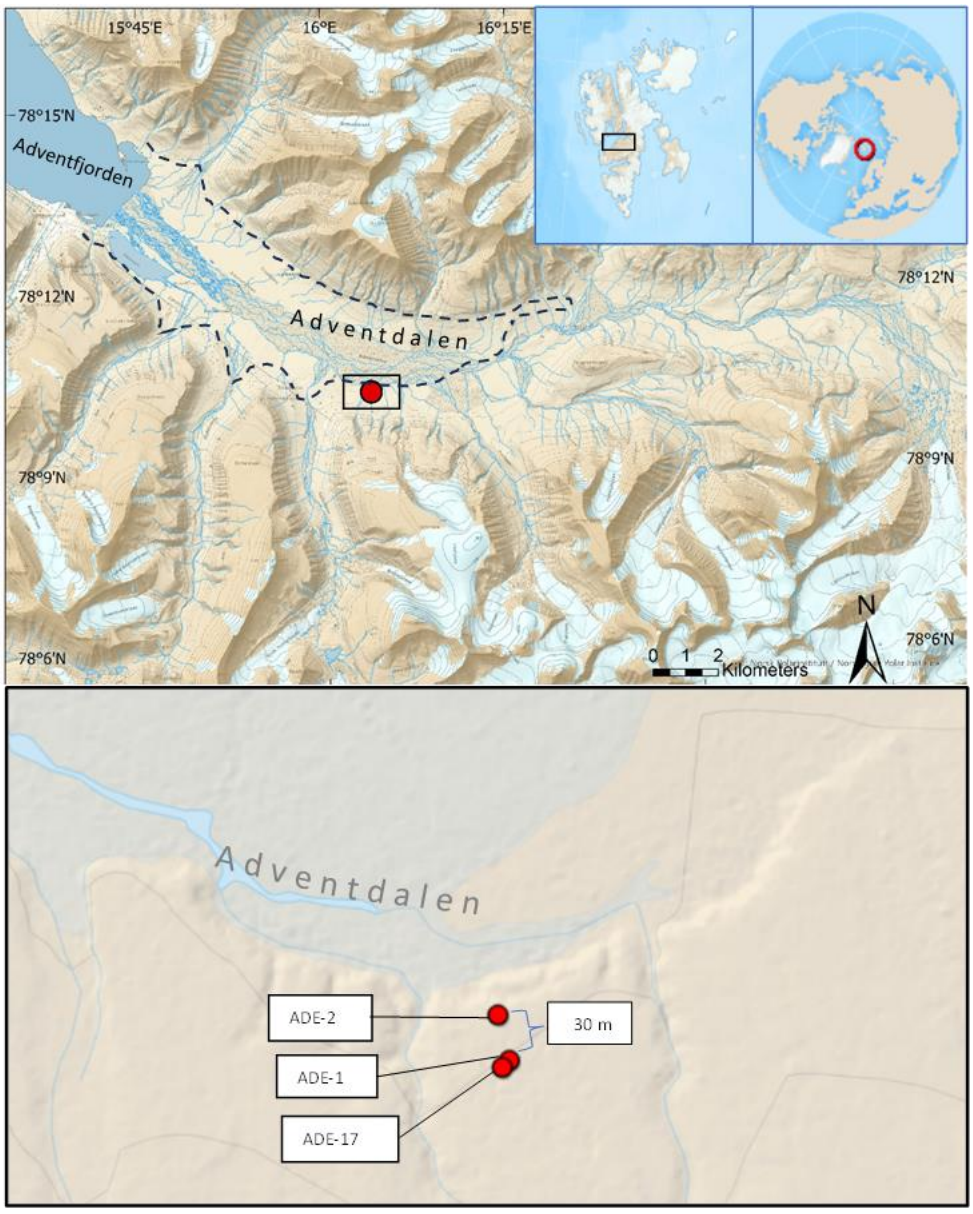

Figure 1: Location and detailed map of the ADE study site. The dashed line represents sea ingression limit at the early Holocene (Lønne and Nemec, 2004, drawn after Hodson et al., 2020). The map is provided with courtesy of the © Norwegian Polar Institute. All rights reserved.

1.1 Radium isotopes

In this work, we report the activities (disintegrations per time) of radium isotopes in ground ice, as well as their radioactive parents (thorium and actinium) on the permafrost sediments. Radium has four naturally occurring isotopes: ^{223}Ra, ^{224}Ra, ^{226}Ra, and ^{228}Ra. All isotopes are produced by decay chains, stemming from ^{238}U, ^{235}U, and ^{232}Th (Fig. 2). Specifically, all Ra isotopes are produced by the α decay of different Th (thorium) isotopes (^{227}Th,

^{228}Th, ^{230}Th, and ^{227}Th, respectively). In the case of ^{223}Ra, we usually relate to its grandparent ^{227}Ac with a half-life of 21.7 years, due to the short life of its direct parent ^{227}Th (half-life: 18.7 days). An important aspect is that thorium (parent isotope) is highly particle-reactive and tends to strongly adsorb onto mineral surfaces, whereas radium is more mobile and is more common in the dissolved phase. Also, the alpha-recoil effect during radioactive decay provides the kinetic energy necessary to eject radium from the mineral lattice into the pore space. The ^{226}Ra is the longest-lived radium isotope, with a half-life of 1601 years; ^{228}Ra has a half-life of 5.75 years, while ^{224}Ra and ^{223}Ra are short-lived, with half-lives of 3.66 and 11.4 days, respectively. The wide range of half-lives of the radium isotopes allows their application to various processes with very different time scales. For example, for short-term groundwater processes, ^{228}Ra, ^{223}Ra, or ^{224}Ra, and their activity ratios are good tracers (e.g., Moore, 2003; Hsieh et al., 2013). However, for a distinction between thawed ground ice and active layer water or between young and old sub-permafrost groundwater, ^{226}Ra would be a better tracer, since its growth toward equilibrium with its parent nuclide, ^{230}Th, takes 5-6 half-lives (8-10,000 years; e.g., Weinstein et al., 2019; Rotem et al., 2024). Radium isotope research in the polar regions has been mostly focused on the land-ocean interface, like shelf-deep basin exchange processes (Rutgers van der Loeff et al., 1994; Kipp et al., 2019, 2023), river discharge as a carrier of carbon and nutrients to the oceans (Rutgers van der Loeff et al., 2002; Bullock et al., 2022) or lakes (Dabrowski, 2020) and direct groundwater discharge to the sea (e.g., Dimova et al., 2015; Charkin et al., 2020). While also studied in relation to soil or river contamination (e.g., Chevychelov and Sobakin, 2017), as tracers of weathering processes (Linhoff et al., 2020), or as part of geological and pedological surveys (e.g., Wojtasik et al., 2017), radium isotopes have just recently been studied as a potential tracer of permafrost degradation-segregation or as a proxy for residence time determination (Weinstein et al., 2019; Kipp et al., 2025). In fact, the only radioisotopes that have previously been used for the determination of ground ice residence time in permafrost soil were uranium isotopes (Ewing et al., 2015) and ^{3}H (for young ice, e.g., Burn and Michel, 1988).

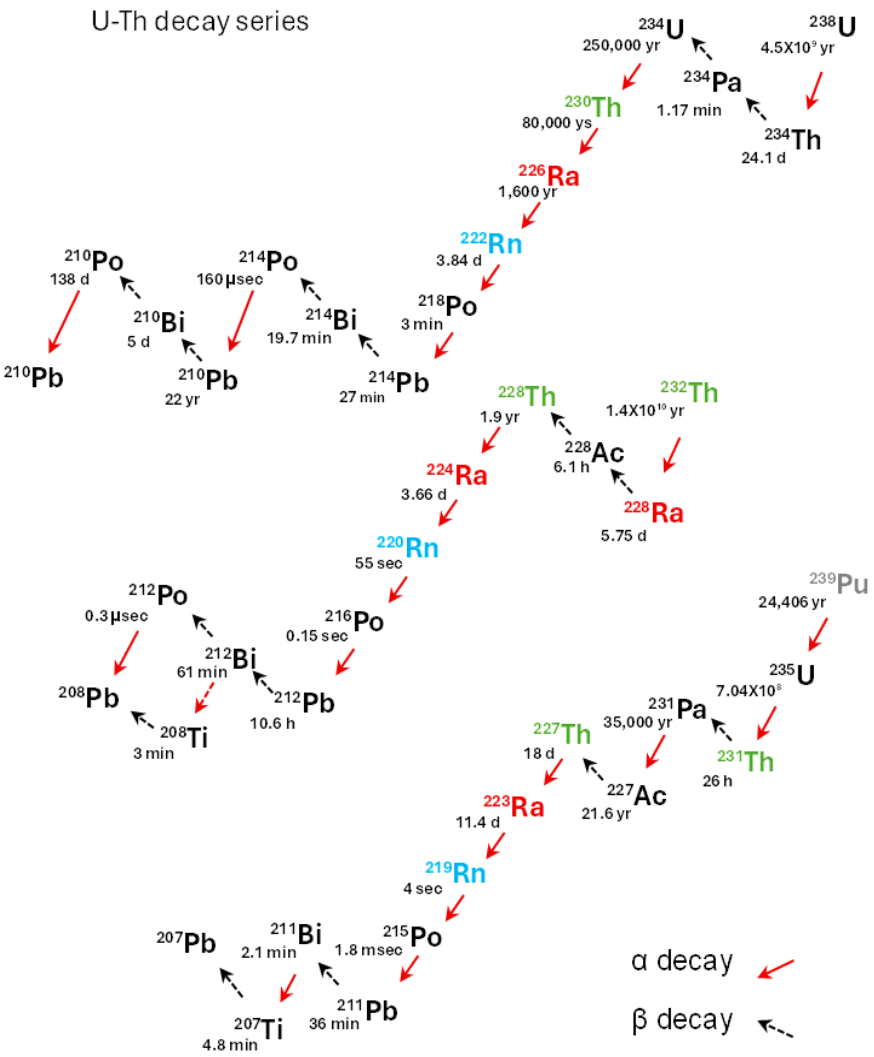

Figure 2: The three U-Th decay series. Radium isotopes are designated red, and Thorium is labelled green. Note that all Ra isotopes are produced by the decay of Th isotopes, and that two of the four Ra isotopes are along the ^{232}Th decay chain.

2. Study site

The data presented in this study are from cores drilled into the permafrost in the Adventdalen Valley (hereafter Adventdalen), Svalbard (Fig. 1), during March 2017 and March 2022. The Adventdalen is a U-shaped fjord valley, carved by advancing and retreating glaciers. During the last glacial cycle, it was eroded to its basement (Elverhøi et al., 1994), which was followed by Early Holocene glacier retreat and seawater ingression up valley (Lønne and Nemec, 2004), resulting in the deposition of deltaic sediments (Gilbert et al., 2018). A relatively fast elastic rebound (Forman et al., 2004) resulted in the exposure of the sediments to the atmosphere, starting at the eastern part of the valley ca. 9.5 ka and arriving at the current coastline location no later than 4 ka (Gilbert et al., 2018). The exposed sediments froze epigenetically within a short time after exposure to the atmosphere (100s of years; Rotem et al., 2023). The marine sediments were then covered by several meters of mid to Late Holocene fluviatile sediments, which were overlain by 2-3 m of aeolian deposits, and both went through syngenetic freezing (Gilbert et al., 2018). At present, the thickness of the permafrost in the valley is estimated at less than 100 m next to the coast (Humlum et al., 2003) and up to 250 m up-valley (Isaksen et al., 2001), most of it being epigenetic and the

shallow 4-5 m syngenetic, while active layer depth ranges between 0.5-1 m (Christiansen et al., 2005; Weinstein et al., 2019). Permafrost in Svalbard is considered continuous (Obu et al., 2019), although non-frozen and partially frozen permafrost were also reported (Keating et al., 2018; Weinstein et al., 2019), and recent works about sub-permafrost hydrology also question the continuity of the permafrost in this area (e.g., Rotem et al., 2024).

Four boreholes were drilled at the ADE site, a river terrace, 23 m.a.s.l, 9.8 km up-valley from the Adventfjorden (Fig. 1). Two closely spaced (0.5 m apart) boreholes, centered at 78.17220N 16.06130E, were drilled during spring 2017, and they are treated here as one core, ADE-17. The other two cores, ADE-1 and ADE-2, were drilled in spring 2022. ADE-1 is located within a few meters from ADE-17 (78.17216N 16.0610E), and ADE-2 was drilled ca. 30 m away (78.17243170N 16.06114840E). The valley-fill section at the site (14-20 m, Gilbert et al., 2018, and this study) consists of 1.5 m of fine-grained aeolian deposits underlain by fluviatile gravel down to 5.5 m, which in turn is underlain by deltaic sediments (ca. 12 m). The Holocene section covers glacial sand deposits, 2.5 m thick (Gilbert et al., 2018), which are underlain by basement rocks (Lower Cretaceous, shales) (Grundvåg et al., 2019).

3. Methods

The drilling campaigns were executed using the University Center in Svalbard (UNIS) permafrost drill rig (Gilbert et al., 2018), using core barrels of 43 mm diameter (ID) in 2017 and 58 mm in 2022. The two boreholes drilled in 2017 reached depths of 13 and 9 m, while the 2022 ones (ADE-1 and -2) reached a depth of 16 m. In the latter, the bottom 1-2 m was composed of bedrock, which was excluded from sample processing. The upper 5 m (syngenetic part) of ADE-2 was drilled with a jackhammer, and the extracted cuttings were analyzed only for chemistry (no Ra isotopes). Core length, borehole depth, core freezing status, and gravel content were recorded in the field. Retrieved core sections were sealed in plastic bags and stored frozen at −18 °C at UNIS. The cores were subsequently sectioned in a cold room (−5 °C) into 0.5–1 m depth intervals. Subsamples were scraped and crushed into small fragments, which were transferred to 250 ml centrifuge tubes. For samples with low water (ice) content, up to 40 ml of Ra-free water was added to facilitate porewater extraction. The samples were then thawed in a microwave oven at 600 W for 2 min and centrifuged for 8 min at 11,000 rpm (high g) to separate the meltwater from the soil matrix. The extracted water was sequentially filtered through 3 µm and 0.45 µm. Net water volumes extracted varied strongly (in accordance with the high variability of ice content) and summed to 42-1391 ml per sample. It is important to note that in this paper, we consider all extracted water as thawed ground ice, although some of the core segments were not fully frozen, thus liquid water could also be present to a certain amount, especially in the more saline samples (see Keating et al., 2018; Weinstein et al., 2019). We also note that centrifuging, as well as the addition of Ra-free water to samples with low ice content, could result in some desorption from grain surfaces, as well as in salt dissolution when it exists. Yet, both salts and adsorbed ions are assumed part of the pore space chemistry (see a similar conception by Ewing et al., 2015, regarding U isotopes in ground ice). Nevertheless, the discussion in this study focuses on Ra isotope ratios, which are less affected by possible desorption. Please also see the discussion of $(^{224}Ra/^{228}Ra)_{AR}$ in section 5.4.

Most of the extracted water was used for Ra isotope analysis, while 30-60 mL was used for elemental chemistry analyses. For Ra isotopes, the solution was run at least three times through columns, filled with 20 g manganese-coated fibers (flow rate of 0.5 l/min). Samples with a pH lower than 6 were pre-treated by adding a low-concentration NaOH solution (Ra-free). Sample water was also run through a secondary Mn-coated fiber to

account for Ra adsorption efficiency. In six samples (DR-AD-121-126), the adsorption efficiency was determined by measuring and comparing ^{226}Ra on both fibers and water samples. Efficiencies were very variable, from 90% down to <50%, with the lower end being mainly due to the relatively low pH and/or reducing conditions. Measured activities of all isotopes were corrected accordingly, assuming no mass-dependent fractionation. Nevertheless, due to the uncertainties about both the extraction protocol and the adsorption efficiency on the fibers, in this paper, we mainly focus on isotope ratios.

The short-lived ^{224}Ra and ^{223}Ra were measured by the RaDeCC system (Moore and Arnold, 1996) within 2-3 days after water-soil separation, while ^{223}Ra was also measured after ca. 10 days, as to check for 220-219 cross-talk interferences (e.g., Diego-Feliu et al., 2020). We note that we found no evidence for cross-talk (i.e., time-corrected activities showed no higher activities during the first compared with the later measurement), which is probably due to the low activities of both isotopes (^{224}Ra was mostly <0.5 cpm). Both ^{224}Ra and ^{223}Ra were corrected for chance coincidence, following Moore and Arnold (1996). ^{224}Ra was re-measured after 3-4 weeks, after reaching equilibrium with its radioactive parent ^{228}Th. Fibers were measured for ^{226}Ra by an emanation system and Lucas Cells (Mathieu et al., 1988) after a 3-week incubation, to allow for ^{222}Rn equilibration with ^{226}Ra. ^{228}Ra was measured by a low-background well-type HPGe gamma spectrometer (Canberra), using the 911 keV peak of ^{228}Ac. All results are presented as dpm (disintegrations per minute) per liter of thawed ground ice, which can change strongly due to the ice content of the permafrost. Analytical errors on ^{226}Ra, ^{228}Ra were ≤7%, while on ^{224}Ra they were ≤13%, and those on the low activity ^{223}Ra averaged 28%, and in two cases exceeded 40% (errors determined, following the protocol of Garcia-Solsona et al. 2008).

The Radium isotopes accumulate in the frozen pore space following recoil from their parent nuclides Th and Ac, which are mostly located either on or within the sediment grains. Accordingly, thorium isotopes and ^{227}Ac were measured both in the bulk grains and in the exchangeable fraction of the permafrost sediment, after thawing and completing the ground ice-soil separation. Several grams of soil samples were disaggregated and homogenized in an agate mortar for the bulk sediment analysis. For the bulk sediment measurements, 0.3 g of each sample was placed in a Teflon beaker and was treated with 1 ml HF and 5 ml HNO_3 (both concentrated, ultrapure grade). A droplet (ca. 0.035 ml) of a ^{229}Th spike (86 ppt) was added to the solution, and the beakers were placed on a hot plate (200 ^{0}C) to let evaporate. The residue was then treated with 5 mL of HCl. A few drops of H_2O_2 were added to treat the organic matter content. The solution was evaporated, and then dissolved by 6 mL 7 N HNO_3. Two ml (out of the 6), dedicated for ^{232}Th and ^{230}Th analyses, were run through Bio-Rad AG 1X8 200-400 mesh resin, following the protocol for thorium ion chromatography separation (Grant et al., 2012). The remaining fraction of 4 ml was buffered with NaOH to pH~7 and kept for ^{228}Th and ^{227}Ac analyses. The exchangeable fraction of thorium and actinium on grain surface was determined by the CEC (Cation Exchange Capacity) ammonium acetate leaching protocol (e.g., Sumner and Miller, 1996). Five grams of sediment was shaken with 25 mL of ammonium acetate overnight. The sample was then centrifuged, and the liquid phase was evaporated, dissolved in 2 mL 7N HNO_3, and run through the Bio-Rad resin (above) for ^{232}Th and ^{230}Th analyses. A second set of 5 g sediment was prepared for ^{228}Th and ^{227}Ac, using the same protocol (albeit no chromatography). ^{230}Th and ^{232}Th (radioactive parents of ^{226}Ra and ^{228}Ra, respectively) were determined by the Neptune Plus Multicollector ICPMS at the Institute of Earth Science, The Hebrew University of Jerusalem. All samples for ^{228}Th and ^{227}Ac were run through 20 g manganese-coated fibers and measured by the RaDeCC system (Moore and Arnold, 1996), assuming equilibrium has been achieved with their short-lived radium isotope daughters. Results are presented as dpm g^{-1}

sediment. Analytical errors for the MC-ICPMS thorium measurements were below 2% and 0.5% for the bulk and exchangeable fractions, respectively. In the RaDeCC measurements, while errors for ^{228}Th were <17% (average of 8%), those of the ^{227}Ac averaged 23% for the exchangeable fraction and 34% for the bulk sediment which is due to the low counts.

Major elements were analyzed at the Geological Survey of Israel (GSI). Cations and SO_4^{-2} were measured by inductively coupled plasma atomic emission spectroscopy (ICP-OES; Optima 5300). The Cl^- concentrations were determined according to their concentration in the solutions; above 50 ppm via potentiometer titration (Metrohm 702 SM Titrino titrator connected to a chlorine electrode), while below 50 ppm by Ion Chromatograph, which was also used for the Br^- concentrations. Bicarbonate was analyzed as alkalinity via titration (analyzed only in 60% of the samples). The analytical error for all majors is less than 5%. We note that the chemistry of ground ice in ADE-17 was already presented in Rotem et al. (2023). Ice content, defined as gravimetric moisture content (W–D)/D × 100, where W and D refer to the wet and dry sample mass (Gilbert et al., 2018).

4. Results

4.1. Ground ice chemistry

Ice content (frozen water mass divided by dry mass) of the samples varied strongly, from 2% to >180% (180% ice content translates into 64% water content), and was, in general, higher in the shallow, syngenetic part (Table C1, Appendix A).

Ground ice (i.e., water extracted from thawed permafrost) chemistry differs strongly between the cores and between the shallow, syngenetic, and the deeper, epigenetic parts of the permafrost profile. In cores ADE-17 and ADE-1, chemistry of the syngenetic ground ice is basically that of fresh water with typical TDS concentrations of <400 mg l^{-1} (Table C1), while ionic ratios of major elements to Cl^- are »1 (e.g., Na/Cl of 1.01-3.58, Figs. 3 and 4). On the other hand, ground ice in the epigenetic section, deeper than 5-5.5m, is mostly brackish to saline, with 450-3,230 mgCl^- l^{-1} (TDS of 900-6,500 mg l^{-1}; note that HCO_3^- and Mg^{2+} were not measured in some of the samples). In ADE-2, salinity is significantly higher (up to 7,960 mg Cl^- l^{-1} and TDS of 17,190 mg l^{-1}), with one outlier (DR-AD-125) reaching >23,000 mgCl^-l^{-1} and TDS of >40,000 mg l^{-1} (Table C1). While the higher salinities were observed at epigenetic depths (>5.5m), salinities in the syngenetic section of ADE-2 were also relatively high (TDS »1000 mg l^{-1}), which reached TDS concentrations >6000 mg l^{-1} at the base of this section (Table C1).

In ADE-17, Cl^- and other major elements show a mixing pattern with depth, with concentrations increasing from 470 mgCl l^{-1} at 6 m to 1,900-3,200 mgCl l^{-1} at 9-12 m (Figs. 3a-e). This is not observed in ADE-2, where high salinities are observed up to the top of the epigenetic section. Unlike Cl^-, the Ca^{+2} does not show any pattern with depth, also in ADE-17, and concentrations in the epigenetic section are similar to those in the syngenetic one (Fig. 3f).

Ion ratios in the ground ice of ADE-17 and ADE-1 vary strongly, with Na/Cl and SO_4/Cl showing up to 3.60 and 0.77, respectively, in the syngenetic section (Figs. 4 and 5a-b), and lower ratios in the epigenetic part (≤2 and ≤0.45, respectively, Figs. 5a-b). On the other hand, in ADE-2 ratios are more uniform, with Na/Cl equivalent ratios similar to that of seawater (0.84-1.02) both in epigenetic and the syngenetic section (except for the shallowest-measured sample, at 3.5 m, with Na/Cl=0.4), and SO_4/Cl (in the epigenetic section) mostly lower than that of seawater (≤0.1, Figs. 4 and 5a-b). Ca/Cl, Mg/Cl, and K/Cl generally show similar patterns, with very high K/Cl

and Ca/Cl in the syngenetic part, while close to seawater ratios in the epigenetic part of the profile, this time in all cores (Figs. 5c-d; one outlier, with very high K and low Ca and Mg at 11m, ADE-2, which could be analytical).

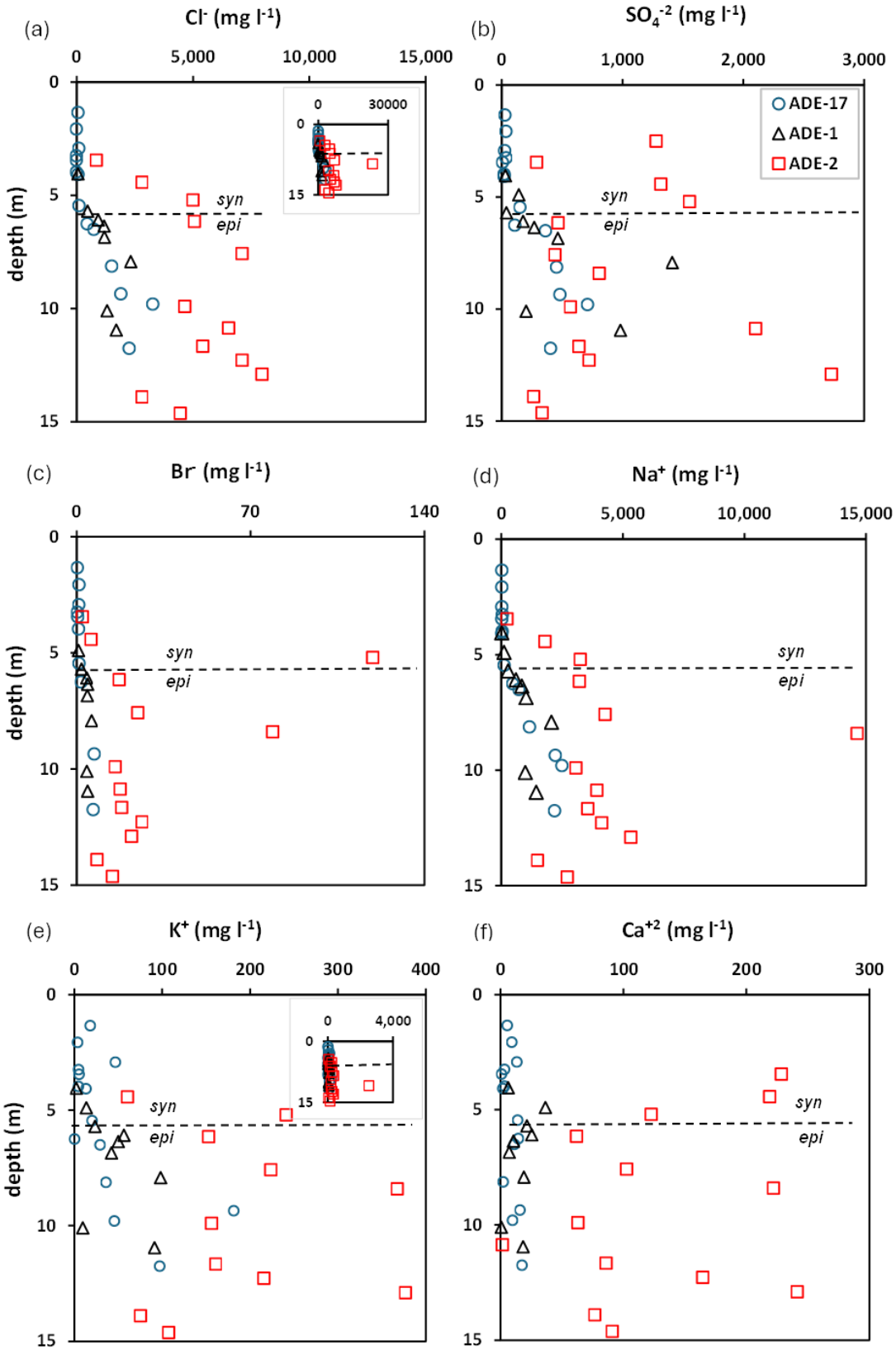

Figure 3: Concentration of selected major elements along the profile of the three ADE cores (ADE-17, ADE-1, and ADE-2). The dashed line shows the boundary between syngenetic *(syn)* and epigenetic *(epi)* permafrost at the site (Gilbert et al., 2018). The insets in the Cl^- and K^+ diagrams are for sample DR-AD-125 and DR-AD-150, respectively.

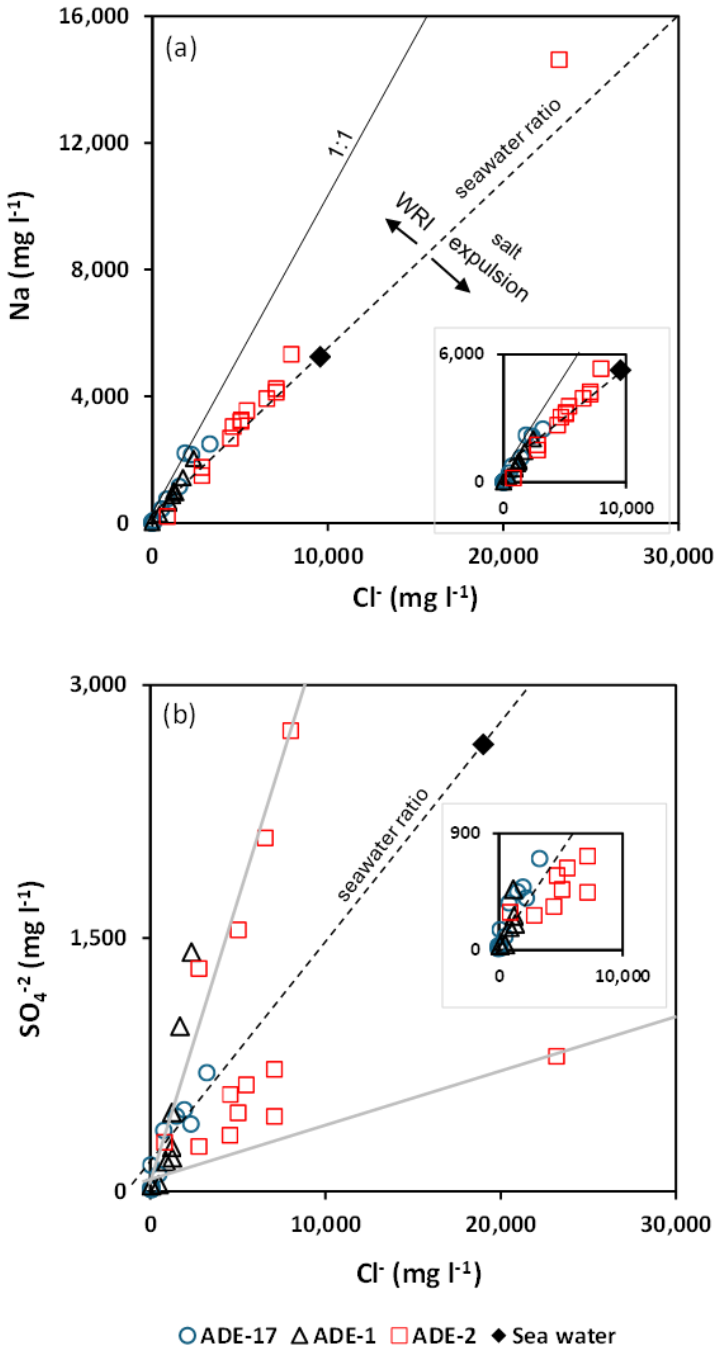

Figure 4: (a) Sodium and (b) sulphate against chloride in the ground ice of the ADE cores. WRI refers to Water-Rock Interaction.

280

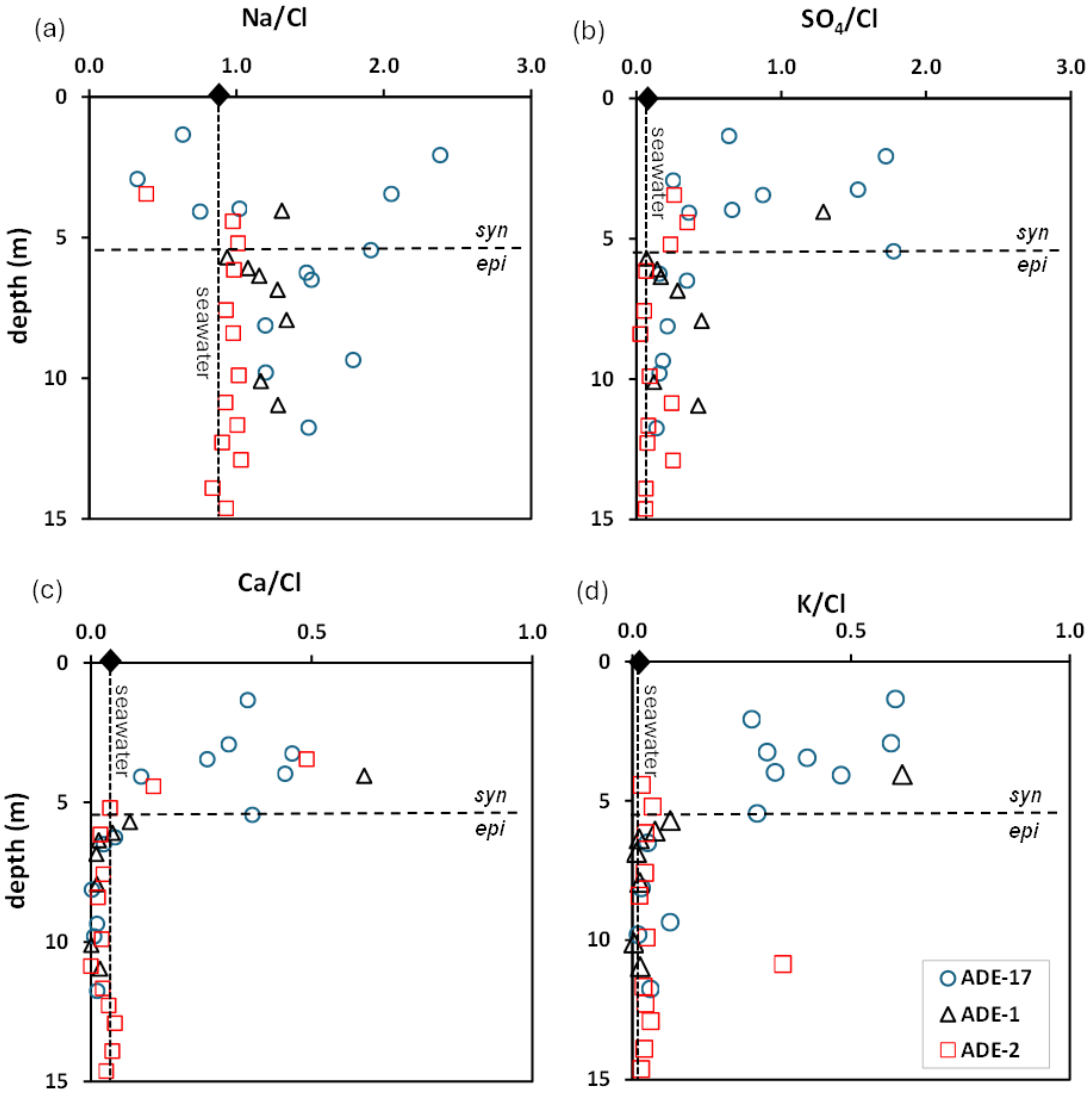

Figure 5: Ground ice equivalent ratios in the ADE cores. The black full diamond and vertical dashed line is for seawater composition (de Baar et al., 2017, Salinity of 35 ppt). The horizontal dashed line as in Figure 3.

4.2. **Radium isotopes in ground ice**

Radium isotope activities in ground ice are presented in Table C2. Activities of ^{226}Ra, ^{228}Ra, and ^{224}Ra in ground ice are quite similar, varying between <1 to 60 dpm l^{-1} (averages of 10-13 dpm l^{-1}), while ^{223}Ra presents much lower activities, with an average of 0.7 dpm l^{-1} (Fig. 6a-d). Activities of ^{224}Ra and ^{223}Ra are fairly uniform and low in ADE-17 and ADE-1 (slightly higher in the epigenetic section), while significantly higher in the more saline ground ice of ADE-2 (epigenetic section; Figs. 6ab, and 7). ^{226}Ra and ^{228}Ra also show higher activities in the epigenetic, compared with the syngenetic section, with no difference between the cores, and with the highest activities observed at the top of the section (6-10 m depth, Fig. 6c-d).

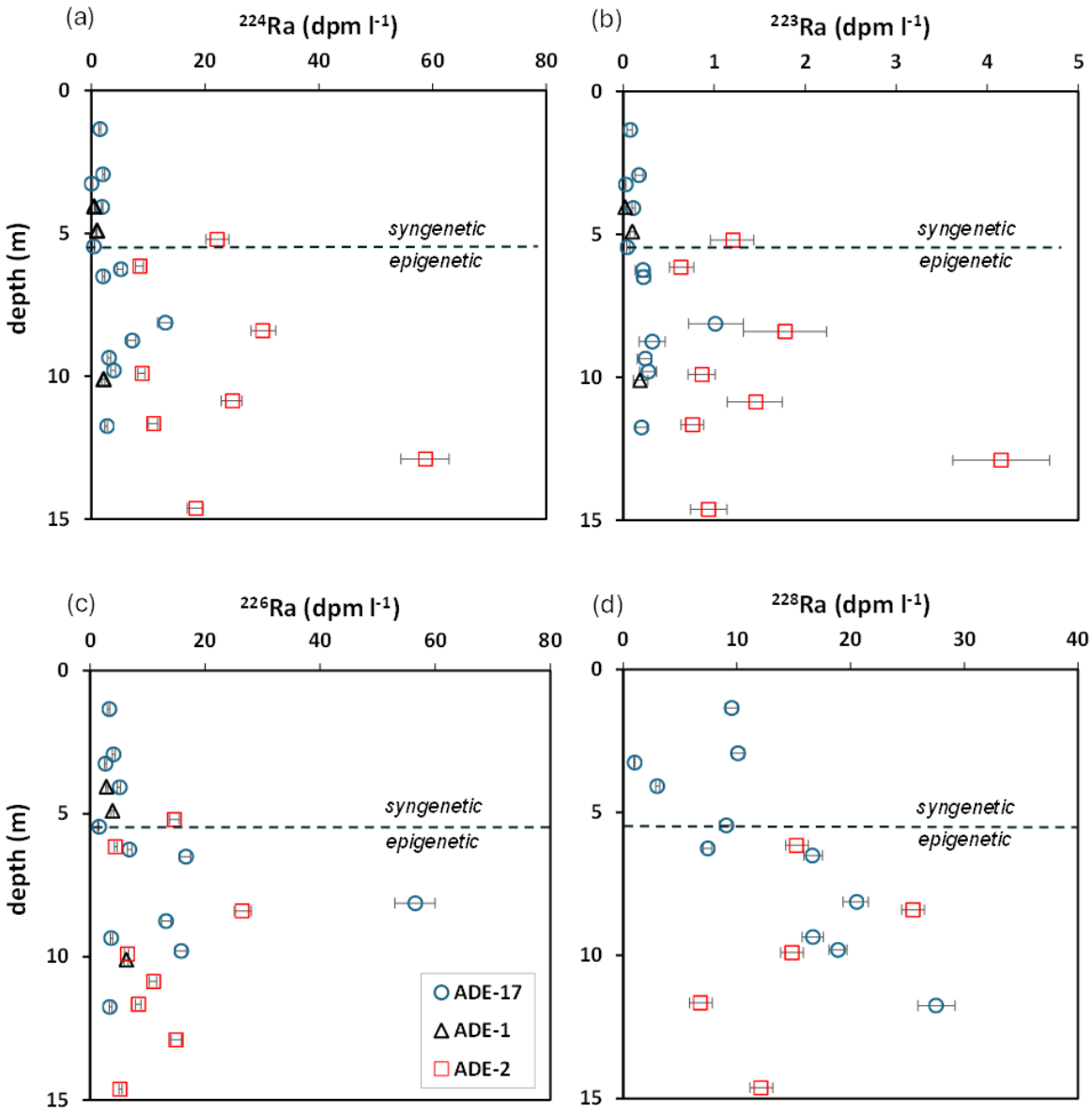

Figure 6: Radium isotope activities in ground ice of the three ADE cores. The dashed line as in Figure 3.

Ratios of the long to short-lived radium isotopes, $(^{226}Ra/^{223}Ra)_{AR}$, demonstrate a large range (4 to 72; Fig. 8a, with three outliers >100) with marked differences between the cores. While in ADE-17 and ADE-1, $(^{226}Ra/^{223}Ra)_{AR}$ ratios both in syngenetic and the epigenetic section are close or higher than the secular equilibrium activity ratio (21.7, which is the natural ratio of parent nuclides $^{238}U/^{235}U$, e.g., Kiro et al., 2015; Weinstein et al., 2021), ratios in ADE-2 (epigenetic section) are relatively low, ranging between 4-14 (Figs. 7c and 8a).

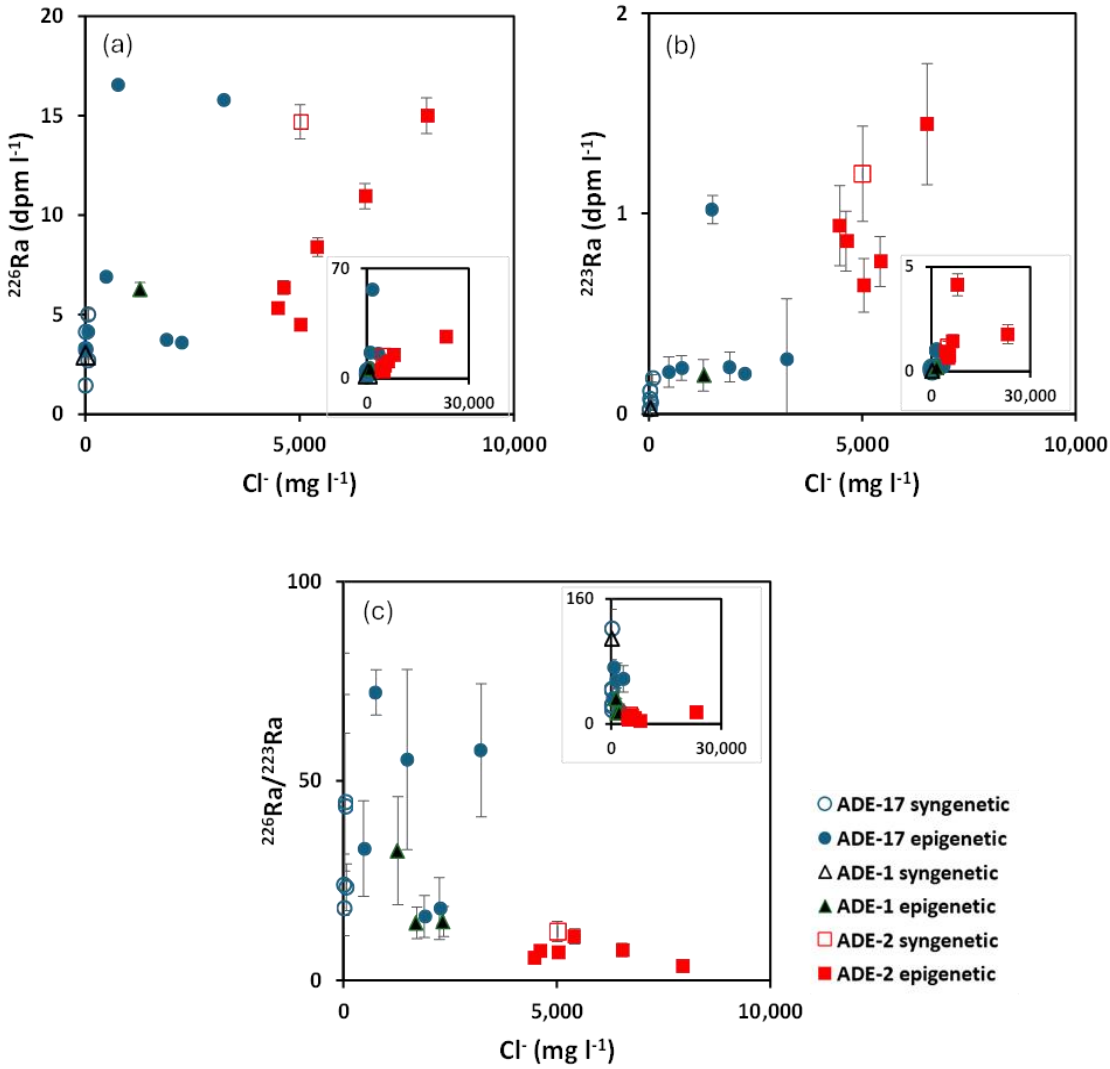

Figure 7: Radium isotope activities and ratios against chloride. (a) ^{226}Ra, (b) ^{223}Ra, (c) ^{226}Ra/^{223}Ra.

($^{226}Ra/^{224}Ra)_{AR}$ shows a similar pattern, where ratios in ground ice from cores ADE-17 and ADE-1 are higher than those in ADE-2 samples (>1and 0.3-1, respectively, Fig. 8b). Ratios of ^{226}Ra to the medium-lived (half-life of 5.75 years) ^{228}Ra are mostly ≤1, with no difference between the cores (Table C2), although some of the ADE-17 samples show ratios >>1. Despite of the much shorter life of ^{228}Ra, $(^{228}Ra/^{223}Ra)_{AR}$ shows a pattern very similar to that of and $(^{226}Ra/^{223}Ra)_{AR}$ (Fig. 8c). Last, the daughter-parent ratio $(^{224}Ra/^{228}Ra)_{AR}$ in ADE-17 ranges between 0.13-0.68, while in ADE-1 and ADE-2, ratios in the epigenetic part are mostly higher (0.55-1.58, Fig. 9).

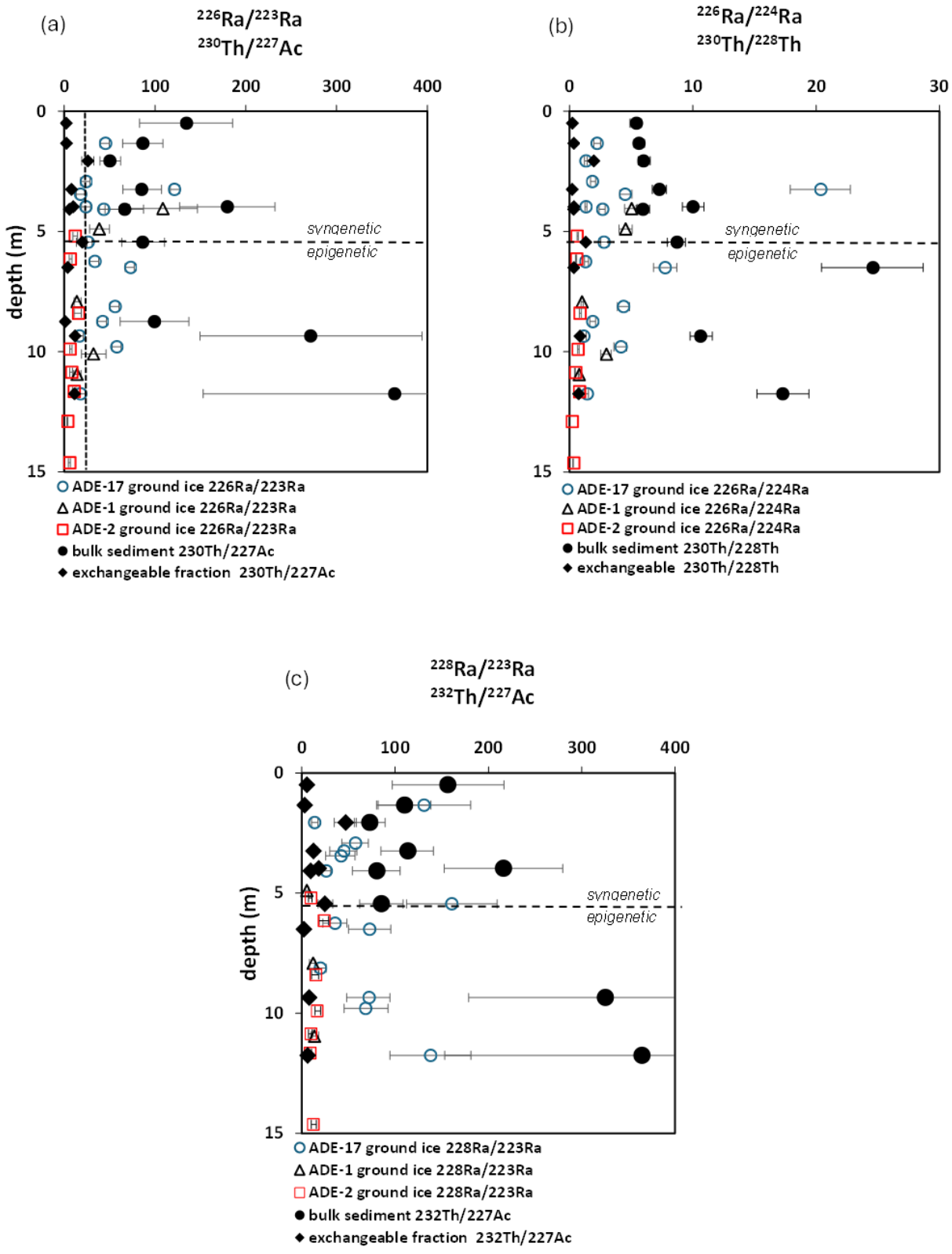

Figure 8: Radium isotope activities in ground ice and their parent ratios in bulk soil grains and on grain surfaces (exchangeable fraction). (a) $(^{226}Ra/^{223}Ra)_{AR}$ and $(^{230}Th/^{227}Ac)_{AR}$; (b) $(^{226}Ra/^{224}Ra)_{AR}$ and $(^{230}Th/^{228}Th)_{AR}$. (c) $(^{228}Ra/^{223}Ra)_{AR}$ and $(^{232}Th/^{227}Ac)_{AR}$. The vertical dotted line in (a) indicates the natural ratio of $(^{238}U/^{235}U)$, parents of ^{226}Ra and ^{223}Ra, respectively. The dashed line as in Figure 3.

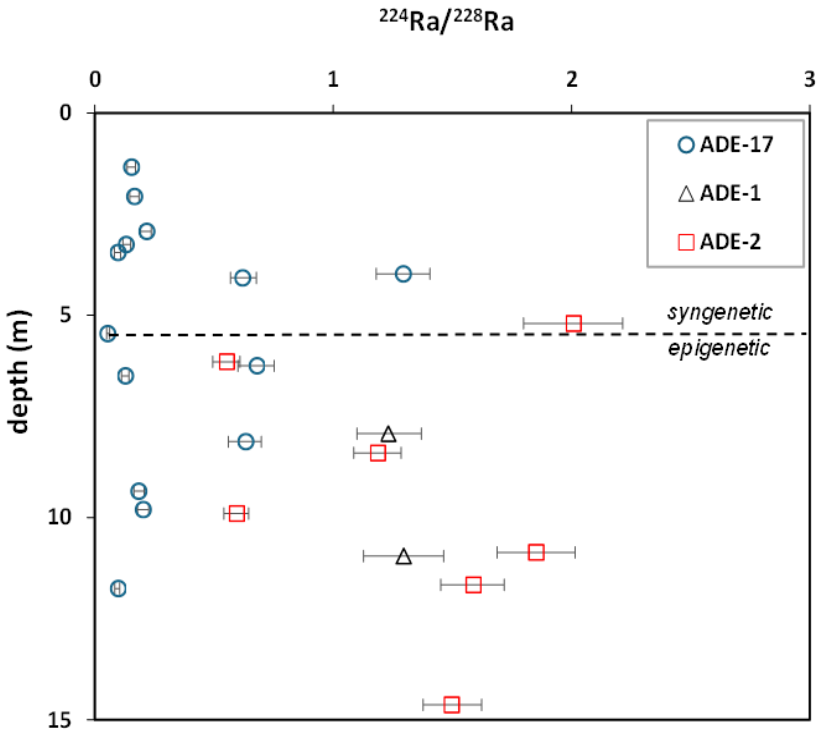

Figure 9: $(^{224}Ra/^{228}Ra)_{AR}$ in the ADE cores. The dashed line as in Figure 3.

4.3. Thorium isotopes and ^{227}Ac in permafrost soil

Thorium isotope activities in soil samples (bulk and exchangeable fraction) from core ADE-17 are presented in Table C3. ^{232}Th and ^{230}Th activities in bulk samples are two to three orders of magnitude higher than in the exchangeable fraction (4.3-8.4 and 0.01-0.17 dpm g^{-1}, respectively), reflecting their main residence inside the grains (mineral lattice). On the other hand, ^{228}Th activities in the exchangeable fraction are similar to those in the bulk (both are in the range of 0.1-1.2 dpm g^{-1}, Table C3 and Fig. 10), implying that most of the latter is adsorbed onto grain surfaces. Importantly, although being progeny of ^{232}Th, ^{228}Th activities are, on average, twice the ^{232}Th activities in the exchangeable fraction. This is due to the fact that ^{228}Th is also produced from ^{228}Ra that recoiled via the decay of ^{232}Th close to grain rims. The above is also true for ^{227}Ac (Table C3), where exchangeable fraction activities are close (though lower) to bulk activities. This is especially true for the epigenetic section, while in the syngenetic part, bulk sediment ^{228}Th is up to 12 times that in the exchangeable fraction (i.e., grain surface ^{228}Th is not dominant, Fig. 10), although still lower than bulk/exchangeable ratios of ^{232}Th and ^{230}Th (10's to 100's, Fig. 10).

$(^{230}Th/^{232}Th)_{AR}$ in the bulk sediment is quite uniform along the whole permafrost section, ranging between 0.7-1.0 (Table C3; Note that these are activity ratios, while concentration ratios average $5x10^{-6}$). Ratios in the exchangeable fraction change from <1 in the syngenetic permafrost to >1 in the epigenetic section (5 – 12 m depth). $(^{230}Th/^{227}Ac)_{AR}$ in bulk sediment are significantly higher than the secular equilibrium activity ratio (21.7, Fig. 8a), while all exchangeable fraction samples show lower than equilibrium activity ratios (2-12, Table C3, and Fig. 8a). The latter is apparently due to the high concentration of ^{227}Ac on grain surfaces. Notably, daughter ratios, $(^{226}Ra/^{223}Ra)_{AR}$ in ground ice of ADE-2 are similar (slightly higher) to the $(^{230}Th/^{227}Ac)_{AR}$ in the exchangeable fraction, while in ADE-17 ratios are much higher, 'mid-way', between the exchangeable fraction and bulk

sediment ratios (Fig. 8a). $(^{230}Th/^{227}Ac)_{AR}$ and $(^{230}Th/^{228}Th)_{AR}$ show a similar pattern, with exchangeable fraction ratios being much lower than the bulk sediment ratios, and with the respective daughter $(^{228}Ra/^{223}Ra)_{AR}$ and $(^{226}Ra/^{224}Ra)_{AR}$ in the ground ice of ADE-2 being similar to the exchangeable fraction parent ratios and those of ADE-17 positioned mostly between exchangeable fraction and the bulk sediment ratios (Fig. 8b-c).

5. Discussion

5.1. The heterogeneous nature of ground ice in Adventdalen

Our study site is located within the reach of the marine early Holocene transgression (Fig. 1, Gilbert et al., 2018), suggesting a-priori that the saline water observed in the permafrost epigenetic section is of an estuary-marine origin. Nevertheless, ground ice retrieved from the same depths in the three cores, located ≤30 m apart (Fig. 1), differ markedly in their salinity and chemical composition, as well as in their radium isotope ratios (Figs. 3-8). The salinity of ground ice from borehole ADE-2 is relatively high, with up to more than seawater salinity and no distinct pattern with depth (Fig. 3). In ADE-17, salinity does not exceed 20% that of seawater, and it increases with depth in the epigenetic section. Finally, in ADE-1, salinity is less than 6-7% that of seawater, and no distinct pattern is observed. The difference between the cores is not just about the extent of dilution with fresh water/ground ice, but also about the contribution of water:rock interaction, as demonstrated by the ionic ratios. While in ADE-2, ionic ratios are relatively similar to seawater (Figs. 4 and 5; although Na/Cl of 1 could indicate halite dissolution in some of the samples and high SO_4/Cl in two of the samples could be due to sulfide oxidation, possibly related to the coal layers, common in the nearby slopes), ground ice from ADE-17 and ADE-1 shows Na/Cl and SO_4/Cl significantly higher than in seawater (Figs. 4 and 5a-b). The similar to seawater chemistry in ADE-2 ground ice favors a marine source for its saline component. On the other hand, the >1 Na/Cl in ADE-17 and ADE-1 (compared

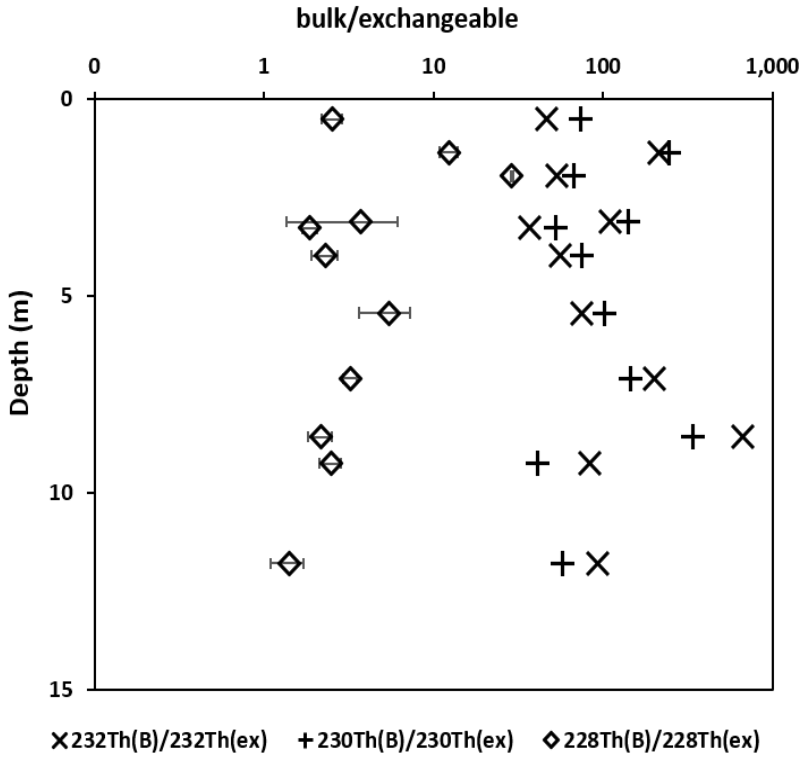

Figure 10: Bulk sediment/exchangeable (B/ex) activity ratios of thorium isotopes in sediments from ADE-17. The dashed line as in Figure 3. Note the logarithmic scale.

with 0.86 in seawater) suggests that, although it probably also contains a seawater component, porewater in these two cores went through significant water-rock interaction (WRI, e.g., dissolution or ion exchange). Accordingly, this water is the result of both mixing between fresh, meteoric water and Early Holocene seawater and of WRI. It should be noted that seawater freezing and saline fluid expulsion could not be a significant player here, since in this case fractionation would result in Na/Cl ratios lower than that of seawater (e.g., Herut et al., 1990), which is hardly observed (see fresh-seawater mixing line in Fig. 4a).

The observation of a high salinity profile in ADE-2 all the way to the top of the epigenetic, marine section could be the result of an immediate freezing following exposure to the atmosphere (e.g., Rotem et al., 2023), which limited mixing with fresh water, as well as reduced the effect of WRI. However, the fact that this profile is very different from the nearby boreholes, including its salinity, composition and pattern with depth, favors a later introduction of saline water into the permafrost pore space at this location, which could occur either via intrusion or by intra-permafrost segregation processes (e.g., Ahonen, 2001; French, 2007; Iwahana et al., 2021). Late Holocene intrusion of a saline fluid is firmly supported by the fact that the high salinity in ADE-2 continues into the syngenetic section (Table 1 and Fig. 3), which has been deposited during 4-2 ka (Gilbert et al., 2018). This will be further discussed in light of the radium and thorium isotope data, as follows.

5.2. Radionuclides insights into ground ice timing

The differences in chemistry between the cores are accompanied by differences in the Ra isotope ratios, where long to short-lived isotope activity ratios ($^{226}Ra/^{224}Ra$, $^{226}Ra/^{223}Ra$ and $^{228}Ra/^{223}Ra$) are significantly lower in the ground ice of ADE-2, compared with those in ADE-17 and ADE-1 (Figs. 8a-c). In particular, while $(^{226}Ra/^{223}Ra)_{AR}$ in ADE-17 and ADE-1 are ≥20, in ADE-2 these ratios are ≤14 (Fig. 8a). The low ratios in ADE-2 are apparently because activities of the short-lived isotopes are significantly higher than in the two other cores (Fig. 6b), while ^{226}Ra activities are quite similar (Fig. 6a). However, the significantly higher salinity in ADE-2 should result in higher activities of all radium isotopes in this core due to the reduced adsorption (e.g., Kraemer and Reid, 1984; Gonneea et al., 2008; Kiro et al., 2012; Vinson et al., 2013), and assuming a non-complete frozen nature of the permafrost (e.g., Gilbert et al., 2019; Keating et al., 2018; Weinstein et al., 2019). The observation that this is the case only with the short-lived isotopes (^{224}Ra and ^{223}Ra), while not with the longer-lived ^{226}Ra and ^{228}Ra, raises the possibility of a timing control on the radium isotopes of ground ice in this core (e.g., Weinstein et al., 2019, 2021), namely that the relatively low ^{226}Ra and ^{228}Ra (compared with ^{223}Ra) is the result of a short residence time of the ADE-2 ground ice. Time constraints will be further discussed below.

Another important observation is that in ADE-2, both $(^{226}Ra/^{223}Ra)_{AR}$, $(^{226}Ra/^{224}Ra)_{AR}$ and $(^{228}Ra/^{223}Ra)_{AR}$ activity ratios in ground ice are similar to (i.e., close to equilibrium with) their parent nuclide activity ratios ($^{230}Th/^{227}Ac$, $^{230}Th/^{228}Th$ and $^{232}Th/^{227}Ac$, respectively) in the exchangeable fraction (i.e., surface of grains). On the other hand, in ADE-17 radium ratios are consistently higher and are closer to parent ratios in the bulk sediment (Figs. 8a-b). We note that while Th and Ac isotope activities were measured only in the ADE-17 sediment, the very close proximity of the cores (within 30 m) and the relatively uniform Th isotope ratios in the exchangeable fraction along the sediment profile (Table C3) suggest that the measured sediment nuclide ratios, in particular the differences between ratios in bulk and the exchangeable fractions, should not be very different between the ADE core locations.

In fact, ^{226}Ra activities in ground ice (1-60 dpm l^{-1}) of all three cores are significantly lower than the ^{230}Th activities in the exchangeable fraction (0.02-0.17 dpm g^{-1}, Table C3), which considering a dry solid density of 2.5 g/cc, a relatively high porosity of 50% (100% ice content, Table C1) and recoil release fraction of 50%, is equivalent to 25-200 dpm l^{-1} (Fig. 11; a more conservative porosity of 25% would triple these activities). The significantly lower ^{226}Ra activities in the ground ice are probably the result of most radium (both ^{226}Ra and other isotopes) being kept on grain surfaces (Fleischer and Raabe, 1978; Suksi and Rasilainen, 1996), either physically attached or adsorbed, if liquid water is present. Notably, ground ice of DR-AD-125, which is characterized by an exceptionally high salinity (Cl^- higher than in seawater, Fig. 4, Table C1), showed unusually high radium activities of all isotopes (Table C2), probably due to lower radium adsorption onto grains.

5.2.1 Ground ice residence times

The similarity between $(^{226}Ra/^{sl}Ra)_{AR}$ (sl = 'short-lived') and $(^{228}Ra/^{sl}Ra)_{AR}$ ratios in ADE-2 and the parent nuclide activity ratios in the exchangeable fraction (Figs. 8a-c) suggests that pore space radium isotopes are in equilibrium with parent nuclides on grain surfaces. Equilibrium activity ratios of radium isotopes are supposed to be achieved within 5-6 half-lives of the longer-lived isotope (e.g., 8-10 kyr for ^{226}Ra; 28-35 years for ^{228}Ra), or shorter if adsorption is involved (Kiro et al., 2013; Weinstein et al., 2021). The concentration of a certain Ra isotope in pore space (water or ground ice) at time t is described by Equation (1), assuming steady production and negligible dissolution and diffusion (e.g., Kiro et al., 2015; Weinstein et al., 2021), as is probably the case in the ground ice.

$$A = \frac{P}{\lambda(K+1)}\left(1 - exp^{-\lambda(K+1)t}\right) + A_0 exp^{-\lambda(K+1)t} \quad (1)$$

A is the activity [dpm l^{-1}] of the isotope, A_0 is the initial activity [dpm l^{-1}] (when the fluid/ice was emplaced in pore space), P is the production by recoil from the sediment [dpm l^{-1} yr^{-1}], λ is the decay constant of the isotope [yr^{-1}], K (=R+1; Krishnaswami et al., 1982) is the unitless adsorption coefficient and t is the time since water (or ice) emplacement in the pore space [yr]. The actual activities of ^{226}Ra and ^{228}Ra in our samples are controlled by adsorption, as well as by the efficiency of the (thawed) ground ice extraction. Accordingly, we prefer to normalize these longer-lived isotopes to ^{223}Ra activities. The short-lived isotopes ^{224}Ra and ^{223}Ra reach steady state activities within weeks, which for the discussed time scales practically means a uniform activity. Therefore, ratios of long to short-lived isotopes solely depend on the initial ratio and on the buildup of the long-lived isotope. Considering the much longer life of ^{226}Ra, it is the equilibrium $(^{226}Ra/^{sl}Ra)$ that should constrain the residence time of the studied ground ice.

In Fig. 11, we show the buildup of $(^{226}Ra/^{223}Ra)_{AR}$ in the ground ice with time. For ^{223}Ra, we make use of the average isotope activity in ADE-2, e.g., 1.4 dpm l^{-1} (Table C2; stdev is 1.1 dpm l^{-1}, which is mainly due to one sample of 3.9 dpm l^{-1}). While C_0 of ^{226}Ra is not well-constrained for the shallow (syngenetic) layers, we assume that fluid in the deeper, epigenetic layers had initial activities similar to that of typical shelf seawater (e.g., 0.1 dpm l^{-1}, Moore, 1996). This is a minimum value, because fluid could reside in pore space much before ground ice formation, but will not change the pattern of buildup to steady-state ratios, as discussed below.

Assuming that ground ice radium in ADE-2 is produced only from the exchangeable fraction, the time that will take $(^{226}Ra/^{223}Ra)_{AR}$ to reach exchangeable $(^{230}Th/^{227}Ac)_{AR}$ is dependent on the adsorption. With K=0 (i.e. R-1), this will take several thousand years. On the other hand, if some liquid is present in pore space (e.g., Keating et al., 2018; Weinstein et al., 2019), this will result in adsorption joining the process, and calculated residence times will significantly shorten. For instance, with K=10, as is the case for seawater salinities (e.g., Weinstein et al.,

2021; Garcia-Orellana et al., 2021; Diego-Feliu et al., 2021), the time to reach equilibrium will be on the order of 100's years, with K=100 times will reduce to 10's years and even less with higher K's. Nevertheless, while timing is not constrained, the relatively low $(^{226}Ra/^{223}Ra)_{AR}$ and $(^{228}Ra/^{223}Ra)_{AR}$ in ADE-2 evidently indicates that there is no significant contribution from inside the grains, where parent activity ratios ($^{230}Th/^{227}Ac$ and $^{232}Th/^{227}Ac$, respectively) are much higher (Figure 8a,c). Below, we use this observation and the circumstantial evidence of the high salinity in the syngenetic section of ADE-2 to infer about the mechanism that is responsible for the higher ratios in the other cores.

As noted, and unlike ADE-2, $(^{226}Ra/^{sl}Ra)_{AR}$ in ground ice of ADE-17 (and ADE-1) are significantly higher than parent nuclide ratios in the exchangeable fraction (e.g., $(^{226}Ra/^{223}Ra)_{AR}$ is mostly 20 - 70), being much closer to (although not in equilibrium with) bulk sediment $^{230}Th/^{227}Ac$ parent ratios (Fig. 8a). This suggests that on top of contribution from the exchangeable fraction, there was enough time in ADE-17 for some ^{226}Ra to arrive from a different source, e.g., from inside the grains. While contribution from the grains could be accomplished by direct recoil from grain rims, there is no reason for this not to happen within the same time scale as that of the exchangeable fraction, which is not the case in ADE-2. Alternatively, we suggest that this contribution is via ^{226}Ra and ^{228}Ra diffusion out of the mineral grains, which is time-dependent. This is discussed in detail in section 5.2.2. Importantly, diffusion from the grains is not relevant for ^{223}Ra, which, with a half-life of 11 days, cannot benefit by diffusion from inside the grains, hence the high $(^{226}Ra/^{223}Ra)_{AR}$ in ADE-17.

The maximum time allowed for ground ice formation in the study site is constrained by the deposition age of the valley-fill marine sediments at the site, which is Early Holocene age (≤10,500 years, e.g., Lønne and Nemec, 2004), and furthermore by the actual permafrost formation (i.e., freezing), which could not occur until elastic rebound allowed exposure to the atmosphere, at 9-9.5 ka (e.g., Gilbert et al., 2018; Rotem et al., 2023). This means that ground ice in ADE-17 could be as old as Early Holocene (9-9.5 ka; note that some authors, e.g. Hornum et al. 2020, argue that permafrost formation has been postponed until about 4 ka). On the other hand, the salinization event in ADE-2 should be much younger, as is evident by the high salinity, documented also in the 4-2 ka syngenetic permafrost (Figs 3 and 4). Below (5.22), we show that the salinization (Ra clock reset) event probably happened much more recently.

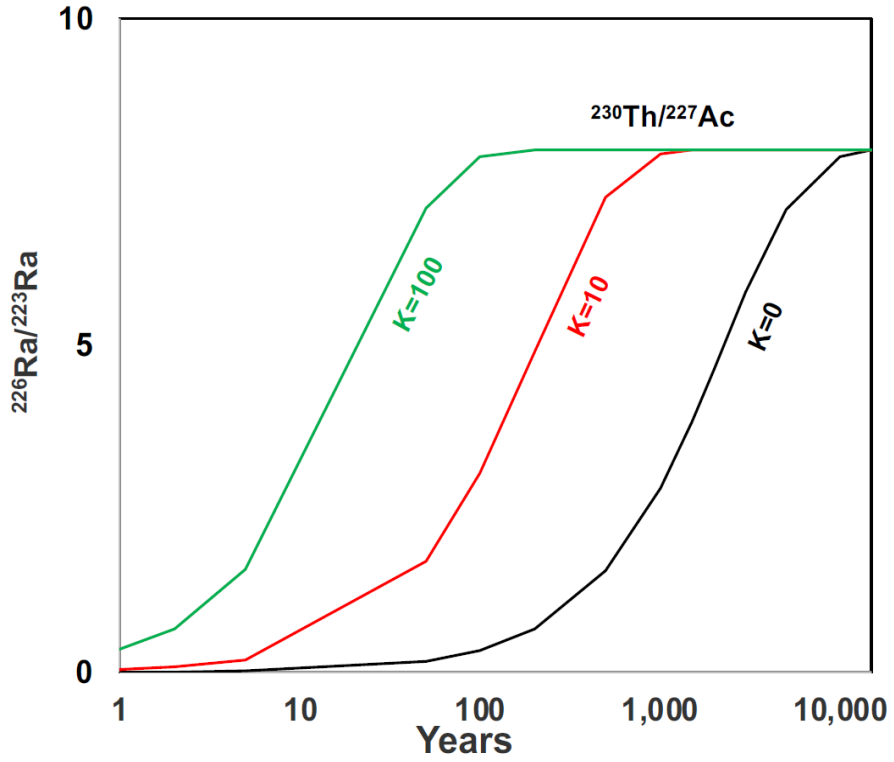

Figure 11: Simulations of the buildup of $(^{226}Ra/^{223}Ra)_{AR}$ in permafrost pore space with different adsorption coefficients (K=0 means no adsorption). See text for further explanations.

510

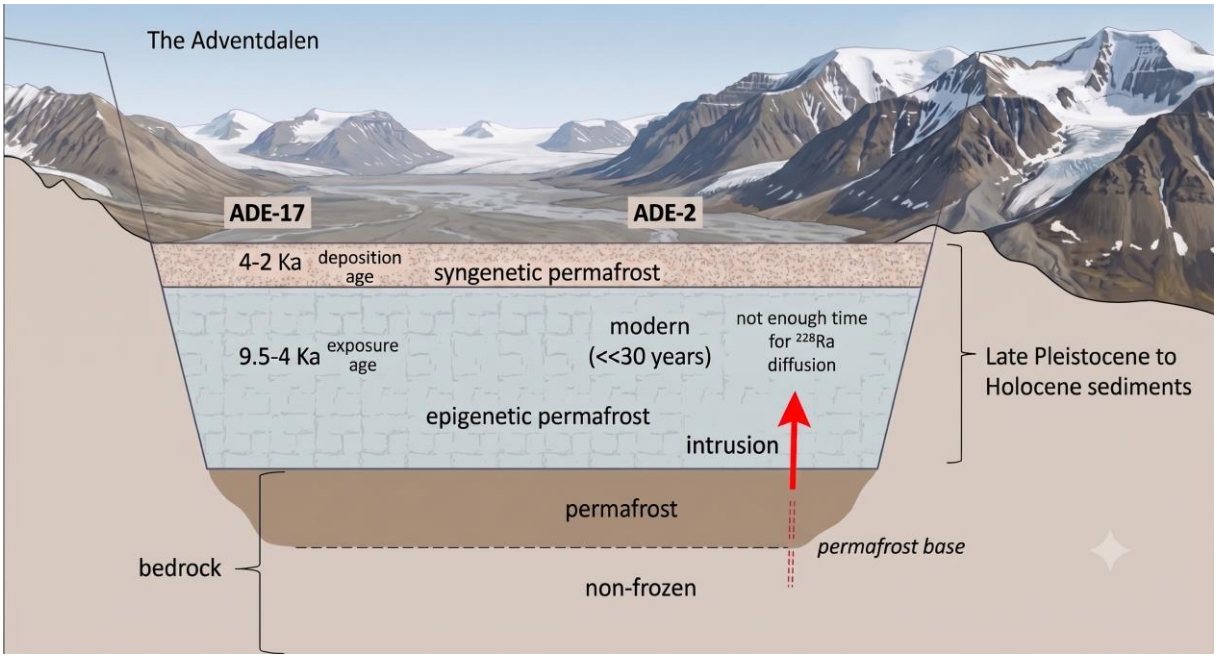

Figure 12. Conceptual model of ground ice versatility and residence times at the ADE site. See text for explanation. Note that locations of ADE-17 and ADE-2 are not to scale. In fact, they are located next to each other (within 30m).

5.2.2 Diffusion from grains in the permafrost

Assuming that diffusion from inside the soil grains controls $(^{226}Ra/^{sl}Ra)_{AR}$ and $(^{228}Ra/^{sl}Ra)_{AR}$ in ground ice, it is the life time of ^{226}Ra and ^{228}Ra that could constrain the residence times involved. While for ^{226}Ra, this could span up to thousands of years, it is the shorter-lived ^{228}Ra that is of interest here. The observation that the ^{228}Ra managed to make its way to pore space in ADE-17 ($^{228}Ra/^{sl}Ra$ closer to equilibrium with bulk sediment parent activity ratios) implies that the effective diffusion time scales are within the time life of this isotope (with half-life of 5.75 years, this practically means up to 20-30 years). Assuming similar sediment composition and texture (same site), this practically means that in ADE-2 there was no time enough even for the ^{228}Ra to diffuse out of the grains, which suggests a very recent 'age' for the ground ice salinization in this core.

Extrapolation from higher temperature data (e.g., for Ca) predicts that D_{Ra} (diffusion coefficients) in sub-zero solids should be very low ($<<10^{-24}$ m^2 sec^{-1}, e.g., Brady and Cherniak, 2010; Cherniak, 2010). This should result in diffusion time scales of at least thousands of years for the 1 μm scale, which practically means that no ^{228}Ra could make its way out of the grains.

Rama and Moore (1984) showed experimentally that radon can diffuse out from sand grains within days, which was attributed to diffusion via nano-pores. On the other hand, they argued that other, non-gaseous nuclides of the U-Th chains could not make it to the intergranular space, and accordingly claimed that this is due to adsorption in the nano-pores. We believe that while radium diffusion could indeed be negligible in the short-term (days to weeks), it is not necessarily the case for the longer term (e.g., years), in particular when silt and clay are considered (unlike the sand and coarser grain size used in Rama and Moore's paper). Accordingly,, we suggest that the actual diffusion follows the nanopore pathway. While diffusion through the ice crystals is probably negligible (D approaches zero), it is commonly believed that the actual diffusion of ions mainly occurs through liquidized (partially melted) ice along grain boundaries (e.g. Jellinek and Chatterjee, 1971; Dash et al. 2006). Hence, we suggest that ^{226}Ra and ^{228}Ra diffuse out of the grains via liquid films, where occur, along nano-pores walls.

In Fig. 13, we used effective diffusion coefficients of 10^{-13} m^2 sec^{-1} and distances relevant to silt (20 μm). Simulations were performed using the following equation: $Ra_p/Ra_g = erfc\{\frac{X}{2*\sqrt{De*\frac{t}{p*R}}}\}$ (Crank, 1975; Bear, 1972), where Ra_p/Ra_g = activity in pore space relative to that in the grain, x=effective distance [m], De=effective diffusion coefficient [m^2 sec^{-1}], t=time [sec], p=porosity [unitless], R=retardation factor [=K+1, unitless, Krishnaswami et al., 1982]. R was assumed 10 for saline water (e.g., Diego-Feliu et al., 2021). Note that the retardation is practically relevant only for liquidized nano-pores.

Molecular diffusion for Ra is assumed similar to that of Ba ($0.85x10^{-9}$ m^2 sec^{-1} at 25°C; Vany´sek, 2017), although Ra^{2+} probably has the largest self-diffusion coefficient in water among the alkaline earth ions, owing to its smallest ionic potential (e.g., Yamaguchi et al., 2022). This should reduce by about an order of magnitude at sub-zero temperature due to the significant increase in water viscosity (Stokes-Einstein relation). Since liquid water is probably highly uncommon in the nano-pores, owing to its low water:rock ratio, we used a much lower intrinsic effective distribution of 10^{-13} m^2 sec^{-1}. Diffusion along grain boundaries is considered as diffusion in veins, where porosity=1. We assumed that the liquid in grains is fresh water, therfore the high R's (K's up to 10^6, e.g., Kumar et al., 2020) used in Figure 13.

The results show that radium could escape silt-size grains within years, assuming the partly (slightly) liquidized nano-pore concept. We suggest that this is the way that both ^{226}Ra and ^{228}Ra are enriched and produce the high long:short-lived ratios in ADE-17. The observation that high ratios are not observed in ADE-2 (note: long-lived activities are similar to ADE-17, but this is apparently due to the ground ice's higher salinity in ADE-2) is probably due to its short residence time (years). Namely, the salinization had to occur quite recently (the actual timing is practically dependent on the effective diffusion coefficient).

Interestingly, ^{228}Ra/^{223}Ra and ^{226}Ra/^{223}Ra show a similar pattern in ADE-17 (compare Figure 8a and 8c), despite of the significant difference in their half-lifves. This suggests that in this core, it is the diffusion pathways (i.e. the liquidized fraction of nano-pores), rather than time, that practically limits Ra diffusion out of the grains. As a matter of fact, only a small fraction of the in-grain produced ^{226}Ra had to diffuse out of the grains in order to produce the high (^{226}Ra/^{sl}Ra)AR. With a bulk ^{230}Th of 4-8 dpm/g (Table C3), a dry density of 2.5 g/cc, porosity of 25-50% (i.e., 50-100% ice content, Table C1) and 50% emanation (release to pore space), ^{226}Ra in ground ice should be as high as 5,000-30,000 dpm/l, which is 2-3 orders higher than that observed in the ground ice (Table C2). Similar calculation could be shown for ^{228}Ra. This probably means that diffusion is quite limited also in ADE-17, probably due to the frozen nature of most nano-pores.

Diffusion time constraints are further illustrated by the ground ice in ADE-1. While $(^{226}Ra/^{sl}Ra)_{AR}$ in this core are similar to shoes in ADE-17, its $(^{228}Ra/^{sl}Ra)_{AR}$ are actually very similar to those of ADE-2. This probably means that in this location (within 10's meters), diffusion has been slower, therefore ^{228}Ra could not practically make it to the pore space.

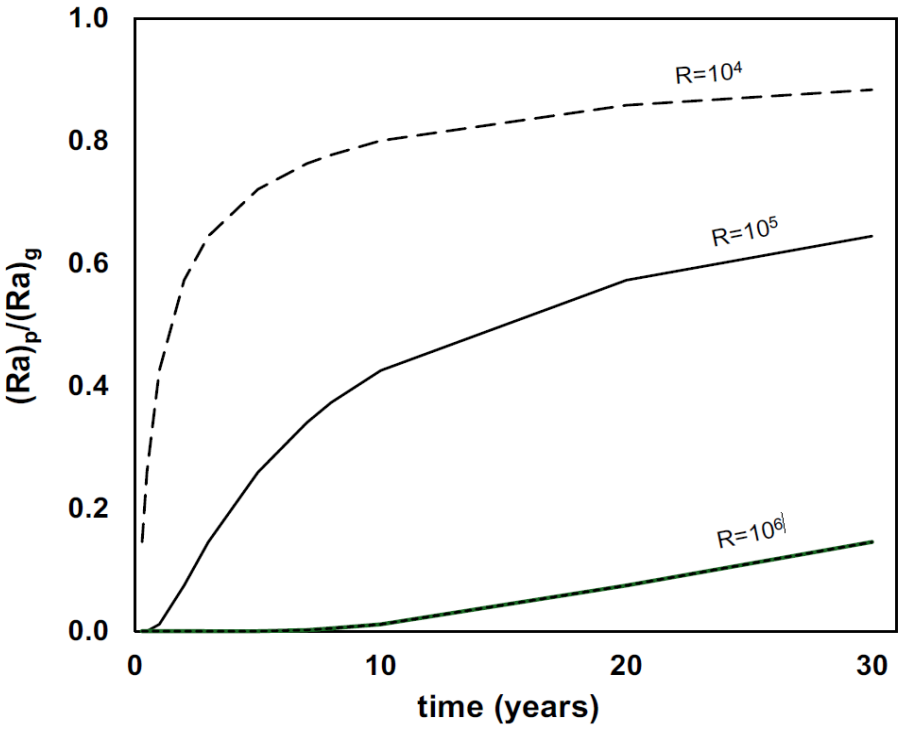

Figure 13: Simulations of diffusion from sediment grains into the pore space. (Ra)p/(Ra)g = Ra activity in pore space normalized to that in grain. Diffusion assumingly occurs through occasional liquidized ice along in-grain frozen nano-pores. De assumed 10-13 (see discussion in text). Retardation values are 104-106 to cover for fresh water at low T.

5.3. Sources of ground ice and permafrost dynamics

The co-existence of pore fluids (ground ice) with different chemistry and supposedly distinct history (residence time) at the same site and depth (from the surface), and the comprehension that ground ice formation (or regeneration) along the profile of one of the cores (ADE-2) is very young, calls for dynamic visualization of the permafrost at Adventdalen. Fluid intrusion and segregation in permafrost has been commonly documented (e.g., French, 2007). This often involves brine intrusion and the formation of cryopegs (e.g., Colangelo-Lillis et al., 2016; Stephani et al., 2020). Fluid migration could be old (millenia and more, e.g., Gilchinsky et al. 2003; Iwahana et al., 2021), but sometimes are apparently young and even very recent (e.g. <1 year, Weinstein et al., 2019).

Rotem et al. (2023) suggested that the saline water (and the frozen fresh-saline water interface) found at the top of the epigenetic section in ADE-17, at >10 m.a.s.l, has been preserved due to the immediate formation of permafrost following seawater regression from this site, ca. 9 ka. It is also apparent that some of the water went through water:rock interaction while in the sediment, probably prior to freezing (e.g., high Na/Cl and SO_4/Cl, Fig. 5), possibly when still covered with seawater.

Accordingly, the similar to seawater composition of the ground ice at ADE-2 and its implied short residence time is quite enigmatic. A direct active connection to the nearby fjord, the Adventfjorden (Fig. 1) via sub-permafrost groundwater flow (i.e., seawater circulation) is unlikely, considering the distance from the fjord (~10 km). With basement geology of shales underlain by sandstones (e.g., Ogata et al., 2014) and a relatively low hydraulic gradient (ca. 2‰, assuming it is parallel to the topographic gradient), the flow rate should not be much more than 1 m y^{-1} (e.g., Hornum et al., 2020), which would result in residence times of several thousand years at the study site. Thus, it seems that salinization and the low $(^{226}Ra/^{sl}Ra)_{AR}$ at ADE-2 are the result of local fluid intrusion and a recent Ra clock reset ('apparent' residence time), rather than the 'real' residence time in the aquifer.

The buildup of radium isotope activity in the pore space, whether hosting water or ground ice, depends on several factors, including (1) the mineralogy of aquifer solids, (2) grain size, and (3) pore space:solid ratio. The migration of water from Th-poor to a Th-rich lithology, as well as from high water:rock to a low water:rock ratio environment, should result in an increased supply of radium, therefore possibly in the reset (or a partial reset) of the Ra isotope-ratio clock. Impact on radium release and resultant reset will be even stronger, if the intruding water is more saline than the older one (assuming a non-completely frozen environment), therefore reducing the adsorption effect. Accordingly, it is suggested that the ground ice in ADE-2 recently experienced a local intrusion of saline water, which previously resided in a low-Th or a high water:rock ratio aquifer. Such an aquifer could be the Early Cretaceous sandstone Helvetiafjellet Formation, which is located >70 m beneath the surface at the site (ca. 60 m below the Adventdalen sediment fill, e.g., Ogata et al., 2014), although the possibility of a deeper source (e.g., the Triassic to Early Jurassic fractured sandstone Geerdalen Formation; Mulrooney et al., 2018) could not be excluded. Sandstone, in particular, fractured, usually has a high water:rock ratio, as well as a low thorium content, compared with the silt-dominated sediments that comprise the valley infill. Sandstone could also explain the limited water-rock interaction, which is demonstrated by the similarity to seawater composition in the ADE-2 ground ice (Fig. 4). Logs taken at deep boreholes in Adventdalen, albeit closer (5 km) to the sea, indicated that groundwater salinity in the Helvetiafjellet Formation (and deeper) is ≥20 mS/cm (~40% seawater conductivity; Braathen et al., 2012), which could also be the case in the basement rocks beneath the ADE site.

The ascent of water from the sub-permafrost zone is demonstrated in Svalbard by artesian discharge, associated with the common pingo structures, in particular in the vicinity of our Adventdalen site (e.g., Demidov et al., 2019;

Hodson et al., 2020; Rotem et al., 2024). This discharge is controlled either by hydraulic heads from the surrounding mountains or by basal permafrost aggradation (e.g., Hornum et al., 2020). Intra-permafrost intrusion or segregation events were also documented in various environments (e.g., French, 2007; Weinstein et al., 2019), sometimes related to non-frozen cryopeg lenses (e.g., Stephani et al., 2020; Iwahana et al., 2021). Although not a massive ice body, like in the common segregated and intrusive ice (e.g., Humlum et al., 2003; Demidov et al., 2021), it is proposed that the very young (modern) ground ice of ADE-2 was formed by saline fluids that arrived from the underlying sandstone reservoir (Fig. 12), possibly forced by the same hydraulic pressure that drives artesian discharge in the nearby pingos (e.g., Hornum et al., 2020). These fluids have been emplaced (intruded) and mixed with ground ice in the shallower permafrost zone in a fingering style, which resulted in the local heterogeneity at the ADE site.

We note that since ground ice analysis has been performed on large core segments (length >0.5 m) and considering the very variable salinity (e.g., 2,000 to >20,000 mgCl l^{-1} in the epigenetic zone, Fig. 3a), we do not have a good resolution of the actual distribution of the saline ground ice. By this we mean the high salinity observed is in fact due to small pockets of very high salinity, where the fingering intrusive fluids managed to intrude and salinize pore space, as well as to reset its Ra clock. We also have no portrayal of the intrusion pathways, which should be further studied.

5.4 The $^{224}Ra/^{228}Ra$ enigma

The relatively low daughter-parent $(^{224}Ra/^{228}Ra)_{AR}$ (<<1) in permafrost ground ice has been noticed in several cases (Weinstein et al., 2019, in Svalbard; Kipp et al., 2025, in Arctic Canada; and Zhang et al., 2025, worldwide). This is remarkably different from the common steady-state ratios of 1-2, mentioned in most groundwater publications (e.g., Krishnaswami et al., 1982; Davidson and Dickson, 1986; Kiro et al., 2015). Interestingly, low ratios also appear in deep, old brines from coastal Israel (Weinstein et al., 2021). In both cases, this was attributed to the adsorption of ^{228}Th (direct ^{224}Ra parent, ^{228}Ra daughter) onto grain surfaces or aquifer rocks, thereby retaining some of the produced ^{224}Ra on the grains and preventing it from reaching the pore space fluid/ice. This, in turn, required the presence of some non-frozen fluid in the pore space, probably as thin films around the grains, in order to allow the highly particle-reactive thorium to adsorb onto grain surfaces. This is in agreement with the observed partially frozen nature of the permafrost in Svalbard and elsewhere (e.g., Keating et al., 2018; Weinstein et al., 2019).

Nevertheless, the results of this study (Fig. 9) suggest that this is not an across-the-board observation, and that some of the samples show ratios within the 'expected' range of 1-2, although this could be affected by enhanced desorption of high $(^{224}Ra/^{228}Ra)_{AR}$ during sample processing in the lab. High ratios are particularly observed in the deep, epigenetic samples of ADE-2, which could be related to the higher salinity (hence, less adsorption or enhanced desorption) in these samples.

6. Summary and Conclusions

In this paper, we used both chemistry and Ra and Th isotopes to get an insight into the ground ice history and fluid migration in the continuous permafrost of a Svalbard valley. While the dominant control on the contribution of short-lived Ra isotopes into the pore space is the recoil of Th-parent nuclides residing on the soil grain surfaces, the supply of the long-lived ^{226}Ra and ^{228}Ra is also controlled by diffusion out of the soil grains, probably mainly

through slightly liquidized nano-pores. The actual activities of all isotopes are also controlled by adsorption, which in turn is dependent on the existence of liquid water in the pore space under the discussed cryotic conditions. The relatively low $(^{226}Ra/^{sl}Ra)_{AR}$ and $(^{228}Ra/^{sl}Ra)_{AR}$ in the ground ice of one core (ADE-2) and its equilibrium with grain surface ratios of thorium isotope parents, while the much higher Ra isotope ratios in ADE-17, suggest that ground ice in the first is younger, or more precisely – has been recently regenerated, probably as a result of fluid intrusion and Ra isotope clock reset. This fluid was significantly more saline than the original one, as reflected in the higher salinity of this core's ground ice, compared with the other cores. Salinization goes almost all the way to the surface, also demonstrating its recent history. The similarity to seawater composition of this young ground ice suggests that the intruding fluids were less subjected to WRI, which is probably due to the characteristic higher water:rock ratio of its source aquifer, most likely an underlying sandstone formation. On the other hand, the different from seawater composition in the other two cores suggests that the water had a significantly longer history in the valley-fill sediments prior to freezing, which is in accordance with their much longer residence time.

This study demonstrates the heterogeneity of the saline permafrost and highlights its complex history and liability to fluid migration, which is probably also the case in other permafrost terrains. While the suggested intrusion is probably the result of basement-originated fluid intrusion, the salinization process could also be affected by the current cryotic conditions of the shallow permafrost. This further highlights saline permafrost's vulnerability to the ongoing climate change and warming. As Arctic temperatures continue to rise, the degradation of saline permafrost may trigger or allow subsurface fluid mobilization, posing significant risks to infrastructure and accelerating the release of stored carbon to the atmosphere.

Appendices

Tables C1, C2 and C3

Table C1. Chemistry and ice content* of ground ice in the ADE cores, East Adventdalen.
*ice content = ice/dry weight

Sample	permafrost type	depth	Cl^-	Br^-	SO_4^{--}	SiO_2	Na^+	K^+	Sr^{++}	Ca^{++}	Mg^{++}	HCO_3^-	ice content*
ADE-17		m	mg l^{-1}	mg l^{-1}	mg l^{-1}	mg l^{-1}	mg l^{-1}	mg l^{-1}	mg l^{-1}	mg l^{-1}	mg l^{-1}	mg l^{-1}	%
DR-AD-55	Syngenetic	1.3	27.3	0.5	23.5	12.8	11.3	18.1	0.2	5.5	15.5	---	165
DR-AD-58	Syngenetic	2.1	12.7	0.6	29.7	14	19.7	3.8	0.41	8.8	27.8	---	69
DR-AD-52	Syngenetic	2.9	72.1	0.7	24.1	8.8	15.5	46.9	0.61	12.6	35.3	---	88
DR-AD-57	Syngenetic	3.3	14	0.5	29.1	5.9	32.6	4.8	0.13	3.6	7.7	---	170
DR-AD-56	Syngenetic	3.5	9.9	0.3	11.8	5.3	13.2	4.4	0.07	1.5	2.6	---	149
DR-AD-61	Syngenetic	4.0	14.5	0.7	13	11.6	9.5	5.2	0.16	3.6	8.8	---	100
DR-AD-63	Syngenetic	4.1	26.8	---	13.4	29.8	13	14.1	0.13	1.7	2.8	---	131
DR-AD-59	Syngenetic	5.5	65.3	0.6	156.5	19.9	81.2	20.6	0.51	13.5	27.8	---	105
DR-AD-53	Epigenetic	6.3	468.3	2.1	102.4	20.5	449.9	0.7	0.53	14.5	3.6	---	14
DR-AD-64	Epigenetic	6.5	765.3	---	362.5	34.7	750.3	29.1	0.15	11.5	---	---	27
DR-AD-65	Epigenetic	8.1	1491.1	---	446.3	19.3	1154.4	35.6	0.08	1.7	---	---	22
DR-AD-54	Epigenetic	9.4	1896.9	7	483.7	8.5	2209.7	181.9	0.3	16.3	---	---	21
DR-AD-66	Epigenetic	9.8	3229.6	---	704.6	23.2	2498.3	45.8	0.34	9.7	---	---	10
DR-AD-60	Epigenetic	11.8	2246.3	6.6	400.5	19.4	2161.1	97.1	0.53	17.8	---	---	14
ADE-1													
DR-AD-146	Syngenetic	4.1	20	---	34.8	6	17	2.9	0.15	7	3.1	9	182
DR-AD-147	Syngenetic	4.9	---	0.8	139.8	12.9	84.4	13.7	0.67	36.6	17.4	35.1	87
DR-AD-128	Epigenetic	5.7	445	1.9	41.8	8	270	23.6	0.37	21.6	16.4	85.1	35
DR-AD-129	Epigenetic	6.1	902	3.7	176	10.2	626	57.1	0.45	25.5	25	232.1	22
DR-AD-130	Epigenetic	6.4	1157.3	4.2	261.5	10.1	866.9	50.1	0.21	10.5	16.4	197.6	45
DR-AD-131	Epigenetic	6.9	1226.4	4.3	468.6	9.6	1012.7	42.4	0.16	7.7	10.9	143.6	27
DR-AD-149	Epigenetic	7.9	2348.7	5.6	1418	4	2043.6	98.2	0.51	19.4	30.6	227.2	17
DR-AD-123	Epigenetic	10.1	1275.6	4	200.3	9.6	961.3	8.8	0.04	0.7	---	183.9	16
DR-AD-148	Epigenetic	11.0	1718.7	4.2	978.9	7.7	1434.4	90.8	0.5	18.5	24.6	195.2	29
ADE-2													
DR-AD-142	Syngenetic	3.5	827.6	2.4	291.2	16.1	204.6	---	3.6	228.3	70.2	8.3	108
DR-AD-141	Syngenetic	4.4	2778.7	5.9	1320.2	8.2	1756.9	59.8	4.1	218.8	156.3	10.9	108
DR-AD-145	Syngenetic	5.2	5010	119.1	1548.8	8.6	3259.8	241.5	2.57	122.6	176.3	243	23
DR-AD-126	Epigenetic	6.2	5035.7	17.3	465.9	9.3	3209.7	152.8	1.45	61.8	128.9	151	23
DR-AD-132	Epigenetic	7.6	7079.1	24.6	445.7	7.6	4240.9	223.3	2.85	102.4	234.2	45.9	13
DR-AD-125	Epigenetic	8.4	23194.9	78.9	801.9	20.6	14624.5	367	6.03	222.2	366.6	611.9	2
DR-AD-124	Epigenetic	9.9	4616.5	15.8	573.7	7.8	3041.5	156.1	1.69	62.4	110.5	164.5	45
DR-AD-150	Epigenetic	10.9	6521.9	17.6	2094.9	29.3	3928.9	2487.8	---	1.4	7.9	340.4	13
DR-AD-122	Epigenetic	11.7	5420	17.8	631.5	11.5	3552.7	160.2	2.29	85.2	115.2	239.3	12
DR-AD-133	Epigenetic	12.3	7071.5	26	724.5	7.2	4129.4	215.9	4.5	164.3	268.5	66.7	116
DR-AD-151	Epigenetic	12.9	7961.7	22	2729.2	7.3	5329.8	377.7	6.61	240.8	292.6	222.5	20
DR-AD-134	Epigenetic	13.9	2774.2	8.2	266.9	6.3	1505.5	75.8	2.57	77.2	106.7	---	13
DR-AD-121	Epigenetic	14.6	4474.1	14.5	333.9	9.9	2679.3	107.9	4.07	91.3	106.1	191.3	25

675 *ice content = ice/dry weight

Table C2. Radium isotope activities* and ratios in ground ice, ADE cores.

sample	permafrost type	depth	^{223}Ra	^{224}Ra	^{226}Ra	^{228}Ra	^{226}Ra/^{223}Ra	^{226}Ra/^{224}Ra	^{226}Ra/^{228}Ra	^{224}Ra/^{228}Ra	^{228}Ra/^{223}Ra
ADE-17		m	dpm l^{-1}	dpm l^{-1}	dpm l^{-1}	dpm l^{-1}					
DR-AD-55	Syngenetic	1.3	0.07±0.03	1.46±0.15	3.26±0.20	9.53±0.52	44.7±17.3	2.2±0.27	0.3±0.03	0.15±0.02	130.6±50.5
DR-AD-52	Syngenetic	2.9	0.18±0.04	2.16±0.19	4.13±0.25	10.11±0.54	23.33±5.8	1.9±0.2	0.4±0.03	0.21±0.02	57.1±14.2
DR-AD-57	Syngenetic	3.3	0.02±0.01	0.13±0.01	2.71±0.16	0.99±0.05	122.00±39.9	20.3±2.4	2.7±0.2	0.13±0.02	44.6±14.2
DR-AD-56	Syngenetic	3.5	---	---	---	---	18.08±6.8	4.57±0.62	0.44±0.04	0.10±0.01	41.4±15.8
DR-AD-61	Syngenetic	4.0	---	---	---	---	24.00±5.8	1.33±0.13	1.73±0.14	1.22±0.11	13.9±3.5
DR-AD-63	Syngenetic	4.1	0.11±0.02	1.89±0.13	5.01±0.29	3.04±0.16	43.62±7.6	2.6±0.2	1.6±0.1	0.62±0.05	26.5±4.6
DR-AD-59	Syngenetic	5.5	0.06±0.02	0.50±0.05	1.44±0.09	9.00±0.51	25.67±7.7	2.9±0.3	0.2±0.01	0.06±0.01	160.8±48.8
DR-AD-53	Epigenetic	6.3	0.21±0.07	5.02±0.50	6.90±0.41	7.41±0.39	33.05±12.0	1.4±0.2	0.9±0.07	0.68±0.08	35.5±12.8
DR-AD-64	Epigenetic	6.5	0.23±0.07	2.13±0.23	16.54±0.96	16.71±0.83	72.2±22.6	7.8±0.9	1.0±0.08	0.13±0.02	73.0±22.7
DR-AD-65	Epigenetic	8.1	1.02±0.30	12.88±1.23	56.49±3.49	20.44±1.10	55.39±16.7	4.4±0.5	2.8±0.23	0.63±0.07	20.0±6.0
DR-AD-67	Epigenetic	8.8	0.32±0.14	7.04±0.75	13.24±0.82	NA	41.6±18.9	1.9±0.2	---	---	---
DR-AD-54	Epigenetic	9.4	0.23±0.08	3.10±0.30	3.74±0.21	16.67±0.94	16.0±5.2	1.2±0.1	0.2±0.02	0.19±0.02	71.4±23.3
DR-AD-66	Epigenetic	9.8	0.27±0.09	3.83±0.41	15.78±0.98	18.88±0.79	57.7±19.9	4.1±0.5	0.8±0.06	0.20±0.02	69.0±23.6
DR-AD-60	Epigenetic	11.8	0.20±0.06	2.60±0.23	3.60±0.24	27.56±1.64	18.0±5.7	1.4±0.1	0.1±0.01	0.09±0.01	138.0±43.4
ADE-1											
DR-AD-146	Syngenetic	4.1	0.03±0.01	0.59±0.05	2.96±0.17	NA	109.2±37.5	5.0±0.5	---	---	---
DR-AD-147	Syngenetic	4.9	0.10±0.03	0.85±0.09	3.87±0.22	0.57±0.03	39.0±10.9	4.5±0.5	6.82±0.51	1.5±0.17	5.7±1.6
DR-AD-149	Epigenetic	7.9	---	---	---	---	14.7±3.8	---	1.28±0.09	1.24±0.14	11.5±3.1
DR-AD-123	Epigenetic	10.1	0.19±0.08	2.12±0.28	6.26±0.35	ND	32.5±13.5	3.0±0.4	---	---	---
DR-AD-148	Epigenetic	11.0	---	---	---	---	14.4±4.0	---	1.26±0.09	1.3±0.14	14.2±4.1
ADE-2											
DR-AD-145	Syngenetic	5.2	1.20±0.24	22.15±2.04	14.68±0.86	11.03±0.56	12.25±2.5	0.6±0.07	0.82±0.06	1.85±0.16	9.2±1.9
DR-AD-126	Epigenetic	6.2	0.64±0.13	8.44±0.69	4.49±0.24	15.28±0.96	7.0±1.5	0.5±0.05	0.3±0.02	0.55±0.06	23.8±5.2
DR-AD-125	Epigenetic	8.4	1.78±0.46	30.24±2.16	26.56±1.48	25.50±1.13	14.9±3.9	0.9±0.08	1.0±0.07	1.2±0.1	14.3±3.7
DR-AD-124	Epigenetic	9.9	0.86±0.15	8.81±0.63	6.36±0.34	14.84±0.73	7.4±1.3	0.7±0.06	0.4±0.03	0.59±0.05	17.2±3.1
DR-AD-150	Epigenetic	10.9	1.45±0.30	24.64±1.84	10.95±0.64	13.31±0.67	7.6±1.6	0.4±0.04	0.82±0.06	1.85±0.16	9.2±2.0
DR-AD-122	Epigenetic	11.7	0.76±0.12	10.83±0.83	8.39±0.48	6.84±0.23	11.0±1.9	0.8±0.07	1.2±0.08	1.58±0.1	9.0±1.5
DR-AD-151	Epigenetic	12.9	4.15±0.53	58.66±4.25	14.99±0.90	NA	3.6±0.5	0.3±0.02	---	---	---
DR-AD-121	Epigenetic	14.6	0.94±0.20	18.24±1.40	5.32±0.28	12.16±0.35	5.7±1.2	0.3±0.03	0.4±0.03	1.50±0.1	12.9±2.8

*Activities are not presented for samples with Ra adsorption efficiencies lower than 50%.

680

685

Table C3. Thorium isotopes activities and ^{227}Ac in sediments from ADE-17

sample	PF type	depth	^{232}Th	^{230}Th	^{228}Th	^{227}Ac	^{232}Th*	^{230}Th*	^{228}Th	^{227}Ac	$^{230}Th/^{227}Ac$	$^{230}Th/^{227}Ac$	$^{230}Th/^{228}Th$	$^{230}Th/^{228}Th$	$^{230}Th/^{232}Th$	$^{230}Th/^{232}Th$	$^{230}Th/^{227}Ac$	$^{230}Th/^{227}Ac$
			dpm g^{-1}	dpm g^{-1}	dpm g^{-1}	dpm g^{-1}	dpm g^{-1}	dpm g^{-1}	dpm g^{-1}	dpm g^{-1}								
		m	bulk sediment				exchangeable fraction				bulk	exch	bulk	exch	bulk	exch	bulk	exch
DR-AD-51	AL	0.5	5.32±0.11	4.55±0.09	0.85±0.07	0.03±0.01	0.12	0.06	0.26±0.02	0.021±0.004	134±51	2.9±0.5	5.4±0.5	0.24±0.01	0.86±0.02	0.53±0.01	156.9±59.9	5.5±1.0
DR-AD-55	Syn	1.3	5.53±0.11	4.35±0.09	0.77±0.06	0.05±0.01	0.03	0.02	0.07±0.01	0.007±0.003	86±22	2.7±1.0	5.7±0.4	0.27±0.03	0.79±0.02	0.69±0.01	110.1±28.2	3.9±1.5
DR-AD-58	Syn	2.1	6.82±0.14	4.75±0.09	0.78±0.06	0.09±0.02	0.13	0.07	0.04±0.00	0.003±0.001	50±11	25.9±6.6	6.1±0.5	1.94±0.15	0.70±0.02	0.55±0.01	72.8±16.4	46.7±11.9
DR-AD-57	Syn	3.3	6.83±0.14	5.19±0.10	0.71±0.06	0.06±0.01	0.06	0.04	0.15±0.01	0.005±0.001	85±21	7.7±2.2	7.3±0.6	0.25±0.02	0.76±0.02	0.60±0.01	113.0±28.1	13.0±3.7
DR-AD-61	Syn	4.0	6.43±0.13	5.34±0.11	0.53±0.05	0.03±0.01	0.17	0.10	0.28±0.02	0.010±0.001	179±52	10.2±2.1	10.0±0.9	0.35±0.02	0.83±0.02	0.57±0.01	216.3±63.5	17.7±3.7
DR-AD-63	Syn	4.1	6.31±0.13	5.23±0.10	0.88±0.08	0.08±0.03	0.11	0.07	0.23±0.01	0.012±0.003	66±21	5.91±1.3	5.9±0.5	0.29±0.02	0.83±0.02	0.61±0.01	79.9±25.6	9.7±2.1
DR-AD-59	Syn	5.5	4.90±0.10	4.99±0.10	0.58±0.05	0.06±0.02	0.07	0.05	0.04±0.00	0.003±0.001	86±23	19.3±5.9	8.7±0.7	1.35±0.11	1.02±0.03	0.75±0.01	85.4±23.3	25.5±7.8
DR-AD-64	Epi	6.5	7.94±0.16	7.57±0.15	0.31±0.05	—	0.04	0.05	0.19±0.01	0.015±0.002	—	3.6±0.4	24.6±4.1	0.27±0.02	0.95±0.03	1.33±0.01		2.7±0.3
DR-AD-67	Epi	8.8	7.75±0.16	7.09±0.14	0.35±0.05	0.07±0.03	0.01	0.02	0.16±0.01	0.011±0.002	99±37	1.8±0.3	20.1±2.9	0.13±0.01	0.91±0.03	1.75±0.01	108.7±41.5	1.1±0.2
DR-AD-54	Epi	9.4	8.41±0.17	7.03±0.14	0.66±0.06	0.03±0.01	0.10	0.17	0.19±0.01	0.014±0.002	271±122	12.5±1.9	10.7±0.9	0.88±0.05	0.84±0.02	1.69±0.01	325.4±146.6	7.4±1.1
DR-AD-60	Epi	11.8	5.94±0.12	5.93±0.12	0.34±0.04	0.02±0.01	0.06	0.10	0.15±0.01	0.009±0.002	364±211	11.0±2.1	17.3±2.1	0.68±0.04	1.00±0.03	1.61±0.01	364.8±211.5	6.8±1.3

PF = permafrost, AL = Active Layer, Syn and Epi = Syngenetic and Epigenetic permafrost respectively, exch = exchangeable fraction.

*Errors of the exchangeable fraction of ^{232}Th and ^{230}Th are <<0.001

Data availability

Data is available through DOI: 10.6084/m9.figshare.30959015

Author contribution

DR, YW, and HHC planned the drilling campaigns; DR and YW processed the cores and lab work in UNIS Svalbard; DR and YH performed the water and soil fractions chemistry analysis at GSI; AT performed soil fraction analyses at the Hebrew University lab. YW developed the simulations of radium isotopes diffusion from sediment clay grains into the pore space; DR and YW wrote the manuscript. All authors commented on the manuscript.

Competing interests

The authors declare that they have no conflict of interest.

Acknowledgments

We would like to express our gratitude to Ullrich (Ulli) Neuman for leading the 2017 and 2022 drilling campaigns in Adventdalen. Many thanks to Andreas Alexander and Graham L. Gilbert for field assistance, to Danni Rohdent and Mai-Brit Schulte for assistance in the lab, and to Gerd-Irene Sigernes and the UNIS logistics personnel for their great assistance with field and laboratory gear. We are also very thankful to the GSI researchers and technicians Olga Berlin, Galit Sharabi, Dina Shtiber, Keren Weiss, and Anton Vaks, who helped with chemical and Th isotope analysis.

Financial support

The project was funded by the Israel Science Foundation grant ISF163/19, while the drilling campaigns were also supported by an Arctic Field Grant from the Norwegian Research Council, Project Number: 269988 RiS ID: 10664.

References

Abramov, A., Vishnivetskaya, T., and Rivkina, E.: Are permafrost microorganisms as old as permafrost? FEMS Microbiol. Ecol, 97(2). https://doi.org/10.1093/femsec/fiaa260, 2021.

Ahonen, L.: Permafrost: occurrence and physiochemical processes (POSIVA--01-05). POSIVA OY, Finland, 2001.

Åkerman, H. J., and Malmström, B.: Permafrost Mounds in the Abisko Area, Northern Sweden. Geografiska Annaler: Series A, Physical Geography, 68(3), 155–165. https://doi.org/10.1080/04353676.1986.11880169, 1986.

Alekseyev, V.R.: Cryogenesis and geodynamics of icing valleys. Geodyn. Tectonophys. 6 (2), 171–224. https://doi.org/10.5800/GT-2015-6-2-0177, 2015.

Anisimov, O. A., and Nelson, F. E.: Permafrost zonation and climate change in the northern hemisphere: results from transient general circulation models. Clim. Change, 35(2), 241-258. https://doi.org/10.1023/A:1005315409698, 1986.

Banin, A., and Anderson, D. M.: Effects of Salt Concentration Changes During Freezing on the Unfrozen Water Content of Porous Materials. Water Resour. Res, *10*(1), 124-128. https://doi.org/10.1029/WR010i001p00124, 1974.

Bear, J.: Dynamics of Fluids in Porous Media. New York: American Elsevier Publishing Company, 1972. ISBN 0-444-00114-X.

Boike, J., Roth, K., and Overduin, P. P.: Thermal and hydrologic dynamics of the active layer at a continuous permafrost site (Taymyr Peninsula, Siberia). Water Resour. Res., 34(3), 355-363. https://doi.org/10.1029/97WR03498, 1998.

Braathen, A., Bælum, K., Christiansen, H.H., et al.: The Longyearbyen CO_2 Lab of Svalbard, Norway—initial assessment of the geological conditions for CO_2 sequestration. Nor. J. Geol., Vol 92, pp. 353–376. Trondheim 2012, ISSN 029-196X, 2012.

Brady, J. B., and Cherniak, D. J.: Diffusion in Minerals: An Overview of Published Experimental Diffusion Data. Rev. Mineral. Geochem., 72, 899–920. https://doi.org/10.2138/rmg.2010.72.20, 2010.

Brigham-Grette, J., and Hopkins, D. M.: Emergent Marine Record and Paleoclimate of the Last Interglaciation along the Northwest Alaskan Coast. Quat. Res., 43(2), 159-173, 1995.

Brouchkov, A.: Nature and distribution of frozen saline sediments on the Russian Arctic coast. Permafr. Periglac. Process, 13, 83–90. https://doi.org/10.1006/qres.1995.1017, 2002.

Brown, J., O. Ferrians, J. A. Heginbottom, E., and Melnikov, E.S.: Circum-Arctic Map of Permafrost and Ground-Ice Conditions, Version 2 [Data Set]. Boulder, Colorado, USA. National Snow and Ice Data Center, 2002.

Bullock, E. J., Kipp, L., Moore, W., Brown, K., Mann, P. J., Vonk, J. E., Zimov, N., and Charette, M. A.: Radium Inputs Into the Arctic Ocean From Rivers: A Basin-Wide Estimate. Journal of Geophysical Research: Oceans, 127(9), e2022JC018964. https://doi.org/10.1029/2022JC01896, (2022).

Burn, C. R., & Michel, F. A.: Evidence for recent temperature-induced water migration into permafrost from the tritium content of ground ice near Mayo, Yukon Territory, Canada. Canadian Journal of Earth Sciences, 25(6), 909-915. https://doi.org/10.1139/e88-087, 1988.

Cable, S., Elberling, B., and Kroon, A.: Holocene permafrost history and cryostratigraphy in the High-Arctic Adventdalen Valley, central Svalbard. Boreas, 47(2), 423-442. https://doi.org/10.1111/bor.12286, 2018.

Cherniak, D.J.: Cation Diffusion in Feldspars. Reviews in Mineralogy & Geochemistry 72, 691-733. DOI: 10.2138/rmg.2010.72.15, 2010.

Charkin, A. N., Pipko, I. I., Yu. Pavlova, G., Dudarev, O. V., Leusov, A. E., Barabanshchikov, Y. A., Shcherbakova, K. P., Yaroshchuk, E. I., Pugach, S. P., Gulenko, T. A., Goriachev, V. A., Semiletov, I. P., and Zarubina, N. V.: Hydrochemistry and isotopic signatures of sub-permafrost groundwater discharge along the eastern slope of the Lena River Delta in the Laptev Sea. Journal of Hydrology, 590, 125515. https://doi.org/10.1016/j.jhydrol.2020.125515, 2020.

Christiansen, H. H., French, H. M., and Humlum, O.: Permafrost in the Gruve-7 mine, Adventdalen, Svalbard. Norw. J. Geog., 59(2), 109–115. https://doi.org/10.1080/00291950510020592, 2005.

Crank, J.: The Mathematics of Diffusion (2nd ed.). Oxford, UK: Clarendon Press, 1975. ISBN 0-19-853344-6.

Colangelo-Lillis, J., Eicken, H., Carpenter, S. D., and Deming, J. W.: Evidence for marine origin and microbial-viral habitability of sub-zero hypersaline aqueous inclusions within permafrost near Barrow, Alaska. *FEMS* Microbiology Ecology, Volume 92(5), fiw053, https://doi.org/10.1093/femsec/fiw053, 2016.

Dabrowski, J. S.: Radium isotopes and radon-222 as tracers of sediment-water interaction in Arctic coastal and, lacustrine environments (Doctoral dissertation, Massachusetts Institute of Technology).(2020).

Dafflon, B., Hubbard, S., Ulrich, C., Peterson, J., Wu, Y., Wainwright, H., and Kneafsey, T. J.: Geophysical estimation of shallow permafrost distribution and properties in an ice-wedge polygon-dominated Arctic tundra region. Geophys, 81(1). https://doi.org/10.1190/geo2015-0175.1, 2016.

Dash, J.G., Rempel, A.W., and Wettlaufer, J.S.: The physics of premelted ice and its geophysical consequences. Reviews Modern Phys. 78, 695–741, 2006.

Davidson, M.R., and Dickson, B.L.: A porous flow model for steady state transport of radium in groundwater. Water Resour. Res. 22 (1), 34–44, 1986.

de Baar, H.J.W., van Heuven, S.M.A.C., and Middag, R.: Ocean Salinity, Major Elements, and Thermohaline Circulation. In: White, W. (eds) Encyclopedia of Geochemistry. Encyclopedia of Earth Sciences Series. Springer, Cham, 2017.

Demidov, N., Wetterich, S., Verkulich, S., Ekaykin, A., Meyer, H., Anisimov, M., Schirrmeister, L., Demidov, V., and Hodson, A. J.: Geochemical signatures of pingo ice and its origin in Grøndalen, west Spitsbergen, The Cryosphere, 13, 3155–316. https://doi.org/10.5194/tc-13-3155-2019, 2019.

Demidov, V., Wetterich, S., Demidov, N., Schirrmeister, L., Verkulich, S., Koshurnikov, A., Gagarin, V., Ekaykin, A., Terekchov, A., Veres, A., and Kozachek, A.: Pingo drilling reveals sodium–chloride-dominated massive ice in Grøndalen, Spitsbergen. Permafr. Periglac. Process, *32*(4), 572-586. https://doi.org/10.1002/ppp.2124, 2021.

Dickinson, W.W., and Rosen, M.R.: Antarctic permafrost: An analogue for water and diagenetic minerals on Mars. Geology 31 (3): 199–202. https://doi.org/10.1130/0091-7613(2003)031<0199:APAAFW>2.0.CO;2, 2003.

Dobinski, W.: Permafrost. Earth Sci. Rev., 108(3-4), 158-169. https://doi.org/10.1016/j.earscirev.2011.06.007, 2011.

Diego-Feliu, M., Rodellas, V., Saaltink, M., Alorda-Kleinglass, A., Goyetche, T., Martínez-Pérez, L., Folch, A., & Garcia-Orellana, J.: New perspectives on the use of 224Ra/228Ra and 222Rn/226Ra activity ratios in groundwater studies. Journal of Hydrology, 596, 126043. https://doi.org/10.1016/j.jhydrol.2021.126043, 2021.

Dimova, N. T., Paytan, A., Kessler, J. D., Sparrow, K. J., Garcia-Tigreros Kodovska, F., Lecher, A. L., ... and Tulaczyk, S. M.: Current magnitude and mechanisms of groundwater discharge in the Arctic: case study from Alaska. Environmental Science and Technology, 49(20), 12036-12043. https://doi.org/10.1021/acs.est.5b02215, 2015.

Elverhøi, A., Svendsen, J. I., Solheim, A., Andersen, E. S., Milliman, J., Mangerud, J., and Hooke, R. L.: Late Quaternary Sediment Yield from the High Arctic Svalbard Area. J. Geol. 103(1). https://doi.org/10.1086/629718, 1994.

Ewing, S.A., Paces, J.B., O'Donnell, J.A., Jorgenson, M.T., Kanevskiy, M.Z., Aiken, G.R., Shur, Y., Harden, J.W., and Striegl, R.: Uranium isotopes and dissolved organic carbon in loess permafrost: modeling the age of ancient ice. Geochim. Cosmochim. Acta 152, 143–165. https://doi.org/10.1016/j.gca.2014.11.008, 2015.

Fisher, D. A., Lacelle, D., and Pollard, W.: A model of unfrozen water content and its transport in icy permafrost soils: Effects on ground ice content and permafrost stability. Permafr. Periglac. Process, 31(1), 184-199. https://doi.org/10.1002/ppp.2031, 2019.

Fleischer, R. L., and Raabe, O.: Recoiling alpha-emitting nuclei. Mechanisms for uranium-series disequilibrium. Geoch. Cosm. Act., 42(7), 973-978. https://doi.org/10.1016/0016-7037(78)90286-7, 1978.

Forman, S. L., Lubinski, D. J., Ingólfsson, Ó., Zeeberg, J. J., Snyder, J. A., Siegert, M. J., and Matishov, G. G.: A review of postglacial emergence on Svalbard, Franz Josef Land and Novaya Zemlya, northern Eurasia. *Quat. Sci. Rev.*, 23(11-13), 1391-1434. https://doi.org/10.1016/j.quascirev.2003.12.007, 2004.

French H.: The Periglacial Environment. Copyright © 2007 by John Wiley & Sons, Ltd., 2007.

French, H.: Recent contributions to the study of past permafrost. Permafr. Periglac. Process, 19(2), 179-194. https://doi.org/10.1002/ppp.614, 2008.

Fu, Z., Wu, Q., Zhang, W., He, H., and Wang, L.: Water Migration and Segregated Ice Formation in Frozen Ground: Current Advances and Future Perspectives. Front. Earth Sci., 10, 826961. https://doi.org/10.3389/feart.2022.826961, 2022.

Gao, Z., Lin, Z., Niu, F., Luo, J., Liu, M., and Yin, G.: Hydrochemistry and controlling mechanism of lakes in permafrost regions along the Qinghai-Tibet Engineering Corridor, China. Geomorphology, 297, 159-169. https://doi.org/10.1016/j.geomorph.2017.09.020, 2017.

Garcia-Solsona, E., Garcia-Orellana, J., Masqué, P., & Dulaiova, H.: Uncertainties associated with 223Ra and 224Ra measurements in water via a Delayed Coincidence Counter (RaDeCC). *Marine Chemistry*, *109*(3-4), 198-219. https://doi.org/10.1016/j.marchem.2007.11.006, 2008

Garcia-Orellana, J., Rodellas, V., Tamborski, J., Diego-Feliu, M., Van Beek, P., Weinstein, Y., Charette, M., Alorda-Kleinglass, A., Michael, H., Stieglitz, T., and Scholten, J.: Radium isotopes as submarine groundwater discharge (SGD) tracers: Review and recommendations. Earth Sci. Rev., 220, 103681. https://doi.org/10.1016/j.earscirev.2021.103681, 2021.

Gilbert, G. L., O'Neill, H. B., Nemec, W., Thiel, C., Christiansen, H. H., and Buylaert, J. P.: Late Quaternary sedimentation and permafrost development in a Svalbard fjord-valley, Norwegian high Arctic. Sedimentology, 65(7), 2531-2558. https://doi.org/10.1111/sed.12476, 2018.

Gilbert, G., Instanes, A., Sinitsyn, A., and Aalberg, A.: Characterization of two sites for geotechnical testing in permafrost: Longyearbyen, Svalbard., AIMS Geosci., 5(4): 868-885. http://hdl.handle.net/11250/2632119, 2019.

Gilichinsky, D., and Wagener, S.: Microbial life in permafrost: A historical review. Permafr. Periglac. Process, 6(3), 243-250. https://doi.org/10.1002/ppp.3430060305, 1995.

Gilichinsky, D., Rivkina, E., Shcherbakova, V., Laurinavichuis, K., and Tiedje, J.: Supercooled Water Brines Within Permafrost – An Unknown Ecological Niche for Microorganisms: A Model for Astrobiology. Astrobiology, 3(2), 331-341.

Gonneea, M.E., Morris, P.J., Dulaiova, H., and Charette, M.A.: New perspectives on radium behavior within a subterranean estuary. Mar. Chem., 109(3-4), 250–267. https://doi.org/10.1016/j.marchem.2007.12.002, 2008.

Grant, K. M., Rohling, E. J., Ayalon, A., Ramsey, C. B., Satow, C., and Roberts, A. P.: Rapid coupling between ice volume and polar temperature over the past 150,000 years. nature, 491(7426), 744-747. https://doi.org/10.1038/nature11593, 2012.

Grundvåg, S.A., Jelby, M. E., Sliwinska, K.K., Nøhr-Hansen, H., Aadland, T., Sandvik, S. E., Tennvassås, I., Engen, T., and Olaussen, S.: Sedimentology and palynology of the Lower Cretaceous succession of central Spitsbergen: integration of subsurface and outcrop data, Nor. J. Geol., 99, 253–284. https://doi.org/10.17850/njg006, 2019.

Harry, D. G., and Gozdzik, J. S.: Ice wedges: growth, thaw transformation, and palaeoenvironmental significance. J. Quat. Sci., 3(1), 39-55. https://doi.org/10.1002/jqs.3390030107, 1988.

Henkemans, E.: Geochemical Characterization of Groundwaters, Surface Waters and Water-Rock Interaction in an Area of Continuous Permafrost Adjacent to the Greenland Ice Sheet, Kangerlussuaq, Southwest Greenland. A thesis presented to the University of Waterloo, Waterloo, Ontario, Canada. http://hdl.handle.net/10012/10193, 2016.

Herut, B., Starinsky, A., Katz, A., and Bein, A.: The role of seawater freezing in the formation of subsurface brines, Geochim. Cosmochim. Acta., 54, 13–21. https://doi.org/10.1016/0016-7037(90)90190-V, 1990.

Hivon, E. G., and Sego, D. C.: Distribution of saline permafrost in the Northwest Territories, Canada. Can. Geotech. J., 30, 506– 514. https://doi.org/10.1139/t93-043, 1993.

Hodson, A. J., Nowak, A., Hornum, M. T., Senger, K., Redeker, K., Christiansen, H. H., Jessen, S., Betlem, P., Thornton, S. F., Turchyn, A. V., Olaussen, S., and Marca, A.: Sub-permafrost methane seepage from open-system pingos in Svalbard, The Cryosphere, 14, 3829–3842. https://doi.org/10.5194/tc-14-3829-2020, 2020.

Hornum, M. T., Hodson, A. J., Jessen, S., Bense, V., and Senger, K.: Numerical modelling of permafrost spring discharge and open-system pingo formation induced by basal permafrost aggradation. The Cryosphere, 14, 4627–4651. https://doi.org/10.5194/tc-14-4627-2020, 2020.

Hsieh, T., Geibert, W., Stahl, H., Aleynik, D., and Henderson, G. M.: Using the radium quartet (228Ra, 226Ra, 224Ra, and 223Ra) to estimate water mixing and radium inputs in Loch Etive, Scotland. *Limnology and Oceanography*, *58*(3), 1089-1102. https://doi.org/10.4319/lo.2013.58.3.1089, 2013.

Humlum, O., Instanes, A., and Sollid, J. L.: Permafrost in Svalbard: a review of research history, climatic background and engineering challenges. Polar Res, 22(2), 191-215. https://doi.org/10.1111/j.1751-8369.2003.tb00107.x, 2003.

Isaksen, K., Holmlund, P., Sollid, J. L., and Harris, C.: Three deep Alpine-permafrost boreholes in Svalbard and Scandinavia. Permafr. Periglac. Process, 12(1), 13-25. https://doi.org/10.1002/ppp.380, 2001.

Iwahana, G., Cooper, Z. S., Carpenter, S. D., Deming, J. W., and Eicken, H.: Intra-ice and intra-sediment cryopeg brine occurrence in permafrost near Utqiaġvik (Barrow). Permafr. Periglac. Process, 32(3), 427-446. https://doi.org/10.1002/ppp.2101, 2021.

James, M., Lewkowicz, A. G., Smith, S. L., and Miceli, C. M.: Multi-decadal degradation and persistence of permafrost in the Alaska Highway corridor, northwest Canada. Environ. Res. Lett., 8(4), 045013. http://dx.doi.org/10.1088/1748-9326/8/4/045013, 2013.

Jellinek, H.H.G., and Chatterjee, A.K.: Diffusion of radioactive sodium in polycrystalline ice. *physica status solidi (a)*, **4**, 173–179, 1971. https://doi.org/10.1002/pssa.2210040118

Jin, H. J., Chang, X. L., and Wang, S. L.: Evolution of permafrost on the Qinghai-Xizang (Tibet) Plateau since the end of the late Pleistocene. J. Geophys., 112(F2). https://doi.org/10.1029/2006JF000521, 2007.

Jones, B. M., Kanevskiy, M. Z., Parsekian, A. D., Bergstedt, H., Ward Jones, M. K., Rangel, R. C., Hinkel, K. M., and Shur, Y.: Rapid Saline Permafrost Thaw Below a Shallow Thermokarst Lake in Arctic Alaska. Geophys. Res. Lett., 50(22), e2023GL105552. https://doi.org/10.1029/2023GL105552, 2023.

Keating, K., Binley, A., Bense, V., Van Dam, R. L., and Christiansen, H. H.: Combined geophysical measurements provide evidence for unfrozen water in permafrost in the Adventdalen valley in Svalbard. Geophys. Res. Lett., 45(15), 7606-7614. https://doi.org/10.1029/2017GL076508, 2018.

Kipp, L. E., Kadko, D. C., Pickart, R. S., Henderson, P. B., Moore, W. S., and Charette, M. A.: Shelf-Basin Interactions and Water Mass Residence Times in the Western Arctic Ocean: Insights Provided by Radium Isotopes. Journal of Geophysical Research: Oceans, 124(5), 3279-3297. https://doi.org/10.1029/2019JC014988, 2019.

Kipp, L., Charette, M., Robbins, A., Pnyushkov, A., Polyakov, I., and Whitmore, L.: Radium Isotopes as Tracers of Shelf-Basin Exchange Processes in the Eastern Arctic Ocean. Journal of Geophysical Research: Oceans, 128(12), e2023JC020303. https://doi.org/10.1029/2023JC020303, 2023.

Kipp, L., Chaillou, G., Kienast, M., Tamborski, J., and Whalen, D.: Radon and radium isotope signatures on a massive ice- and permafrost-rich coastline. Geochim. Cosmochim. Acta., *403*, 166-181. https://doi.org/10.1016/j.gca.2025.06.014, 2025.

Kiro, Y., Yechieli, Y., Voss, C.I., Starinsky, A., and Weinstein, Y.: Modeling radium distribution in coastal aquifers during sea level changes: the Dead Sea case. Geochim. Cosmochim. Acta., 88, 237–254. https://doi.org/10.1016/j.gca.2012.03.022, 2012.

Kiro, Y., Weinstein, Y., Starinsky, A., and Yechieli, Y.: Groundwater ages and reaction rates during seawater circulation in the Dead Sea aquifer. Geochim. Cosmochim. Acta., 122, 17-35. https://doi.org/10.1016/j.gca.2013.08.005, 2013.

Kiro, Y., Weinstein, Y., Starinsky, A., and Yechieli, Y.: Application of radon and radium isotopes to groundwater flow dynamics: An example from the Dead Sea. Chem. Geol., 411, 155-171. https://doi.org/10.1016/j.chemgeo.2015.06.014, 2015.

Kraemer, T.F., and Reid, D.F.: The occurrence and behavior of radium in saline formation water of the U.S. Gulf coast region. Isotope Geosci, 2, 153-174. https://doi.org/10.1016/0009-2541(84)90186-4, 1984.

Krishnaswami, S., Graustein, W. C., Turekian, K. K., and Dowd, J. F.: Radium, thorium and radioactive lead isotopes in groundwaters: Application to the in-situ determination of adsorption-desorption rate constants and retardation factors. Water Resour. Res., 18(6), 1663-1675. https://doi.org/10.1029/WR018i006p01663, 1982.

Kumar, A., Rout, S., Pulhani, V. et al.: A review on distribution coefficient (Kd) of some selected radionuclides in soil/sediment over the last three decades. J Radioanal Nucl Chem 323, 13–26 https://doi.org/10.1007/s10967-019-06930-x, 2020

Kwong, Y.T.J., and Gan, T.Y.: Northward migration of permafrost along the Mackenzie highway and climatic warming. Clim. Change, 26, 399–419. https://doi.org/10.1007/BF01094404, 1994.

Lacelle, D., Fisher, D. A., Verret, M., and Pollard, W.: Improved prediction of the vertical distribution of ground ice in Arctic-Antarctic permafrost sediments. Commun. Earth Environ. 3(1), 1-12. https://doi.org/10.1038/s43247-022-00367-z, 2022.

Li, G., Zhang, M., Pei, W., Melnikov, A., Khristoforov, I., Li, R., and Yu, F.: Changes in permafrost extent and active layer thickness in the Northern Hemisphere from 1969 to 2018. Sci. Total Environ., 804, 150182. https://doi.org/10.1016/j.scitotenv.2021.150182, 2022.

Lønne, I. and Nemec, W.: High-arctic fan delta recording deglaciation and environment disequilibrium, Sedimentology, 51, 553–589. https://doi.org/10.1111/j.1365-3091.2004.00636.x, 2004.

Mackay J. R.: Downward water movement into frozen ground, western arctic coast, Canada. Can. J. Earth Sci. 20(1): 120-134. https://doi.org/10.1139/e83-012, 1983.

Mackay, J. R.: Ice-Wedge Cracks, Western Arctic Coast. Can. Geogr., 33(4), 365-368. https://doi.org/10.1111/j.1541-0064.1989.tb00923.x, 1989.

Mackay, J. R., and Dallimore, S. R.: Massive ice of the Tuktoyaktuk area, western Arctic coast, Canada. Can. J. Earth Sci., 29(6), 1235-1249. https://doi.org/10.1139/e92-099, 1992.

Marion, G. M.: Freeze-Thaw Processes and Soil Chemistry (No. CRRELSR9512)., 1995.

Marsh, P., and Woo, M. K.: Infiltration of meltwater into frozen soils in a continuous permafrost environment. In Proceedings of the sixth international conference on permafrost, Vol. 1, pp. 443-448. Beijing: South China University of Technology Press, 1993.

Mathieu, G. G., Biscaye, P. E., Lupton, R. A., and Hammond, D. E.: System for measurement of ^{222}Rn at low levels in natural waters. Health Phys., 55(6), 989-992, 1988.

Moore W. S.: Large groundwater inputs to coastal waters revealed by ^{226}Ra enrichments. Nature, 380, 612–614. https://doi.org/10.1038/380612a0, 1996.

Moore, W. S., and Arnold, R.: Measurement of ^{223}Ra and ^{224}Ra in coastal waters using a delayed coincidence counter. J. Geophys. Res. Oceans, 101(C1), 1321-1329. https://doi.org/10.1029/95JC03139, 1996.

Moore, W.S.: Sources and fluxes of submarine groundwater discharge delineated by radium isotopes. *Biogeochemistry* 66, 75–93, https://doi.org/10.1023/B:BIOG.0000006065.77764.a0, 2003.

Mulrooney, M.J., Larsen, L., Van Stappen, J., Rismyhr, B., Senger, K., Braathen, A., Olaussen, S., Mørk, M.B.E., Ogata, K. and Cnudde, V.: Fluid flow properties of the Wilhelmøya Subgroup, a potential unconventional CO_2 storage unit in central Spitsbergen. Nor. J. Geol. 85-116. https://doi.org/10.17850/njg002, 2018.

Obu, J., Westermann, S., Bartsch, A., et al.: Northern Hemisphere permafrost map based on TTOP modelling for 2000–2016 at 1 km2 scale. Earth-Sci Rev, 193, 299-316. https://doi.org/10.1016/j.earscirev.2019.04.023, 2019.

Ogata, K., Senger, K., Braathen, A., Tveranger, J., and Olaussen, S.: The importance of natural fractures in a tight reservoir for potential CO_2 storage: a case study of the upper Triassic–middle Jurassic Kapp Toscana Group (Spitsbergen, Arctic Norway). Geological Society, London, Special Publications, 374(1), 395-415. https://doi.org/10.1144/SP374.9, 2014.

Opel, T., Meyer, H., Wetterich, S., Laepple, T., Dereviagin, A., and Murton, J. Ice wedges as archives of winter paleoclimate: A review. Permafr. Periglac. Process, 29(3), 199-209. https://doi.org/10.1002/ppp.1980, 2018.

Osterkamp, T. E., and Romanovsky, V. E.: Evidence for warming and thawing of discontinuous permafrost in Alaska. Permafr. Periglac. Process, 10(1), 17-37. https://doi.org/10.1002/(SICI)1099-1530(199901/03)10:1<17::AID-PPP303>3.0.CO;2-4, 1998.

Rama and Moore, W.: Mechanism of transport of U-Th series radioisotopes from solids into ground water. *Geochimica et Cosmochimica Acta*, *48*(2), 395-399. https://doi.org/10.1016/0016-7037(84)90261-8, 1984.

Rotem, D., Lyakhovsky, V., Christiansen, H. H., Harlavan, and Weinstein, Y.: Permafrost saline water and Early to mid-Holocene permafrost aggradation in Svalbard, The Cryosphere, 17, 3363–3381. https://doi.org/10.5194/tc-17-3363-2023, 2023.

Rotem, D., Weinstein, Y., Christiansen, H. H., Sültenfuß, J., and Hodson, A.: Ra isotope perspective on the hydrology and continuity of permafrost in the high Arctic. Sci. Total Environ., 950, 175412. https://doi.org/10.1016/j.scitotenv.2024.175412, 2024.

Rutgers Van Der Loeff, M. M., Key, R. M., Scholten, J., Bauch, D., and Michel, A.: 228Ra as a tracer for shelf water in the Arctic Ocean. Deep Sea Research Part II: Topical Studies in Oceanography, 42(6), 1533-1553. https://doi.org/10.1016/0967-0645(95)00053-4, 1994.

Rutgers van der Loeff, M., Kühne, S., Wahsner, M., Höltzen, H., Frank, M., Ekwurzel, B., Mensch, M., and Rachold, V.: 228Ra and 226Ra in the Kara and Laptev seas. Continental Shelf Research, 23(1), 113-124. https://doi.org/10.1016/S0278-4343(02)00169-3, 2002.

Sheshukov, A. Y., and Nieber, J. L.: One-dimensional freezing of non-heaving unsaturated soils: Model formulation and similarity solution. Water Resour. Res., 47(11). https://doi.org/10.1029/2011WR010512, 2011.

Solomatin, V. I., and Xu, X.: Water migration and ice segregation in the transition zone between thawed and frozen soil. Permafr. Periglac. Process, *5*(3), 185-190. https://doi.org/10.1002/ppp.3430050307, 1994.

Stephani, E., Drage, J., Miller, D., Jones, B. M., and Kanevskiy, M.: Taliks, cryopegs, and permafrost dynamics related to channel migration, Colville River Delta, Alaska. Permafr. Periglac. Process, *31*(2), 239-254. https://doi.org/10.1002/ppp.2046, 2020.

Suksi, J. and Rasilainen, K.: On the Role of α-Recoil in Uranium Migration - Some Findings from the Palmottu natural Analogue Site, SW Finland. Radiochim. Acta, 74(s1), 297-302. https://doi.org/10.1524/ract.1996.74.special-issue.297, 1996.

Sumner, M. E., and Miller, W. P.: Cation exchange capacity and exchange coefficients. In D. L. Sparks et al. (Eds.), Methods of Soil Analysis, Part 3: Chemical Methods (pp. 1201–1229). Soil Science Society of America, Madison, WI., 1996.

Vany´sek, P.: Ionic conductivity and diffusion at infinite dilution. In: Haynes, W.M. (ed.), CRC Handbook Of Chemistry and Physics. CRC Press, Taylor & Francis Group, 6000 Broken Sound Parkway NW, Suite 300, Boca Raton, FL 33487-2742, 2017.

Vinson, D.S., Tagma, T., Bouchaou, L., Dwyer, G.S., Warner, N.R., and Vengosh, A.: Occurrence and mobilization of radium in fresh to saline coastal groundwater inferred from geochemical and isotopic tracers (Sr, S, O, H, Ra, Rn). Appl. Geochem. 38, 161–175. http://dx.doi.org/10.1016/j.apgeochem.2013.09.004, 2013.

Wang, S., Wang, Q., Xu, J., and Ding, J.: Effect of freeze-thaw on freezing point and thermal conductivity of loess. Arab. J. Geosci., 13:206. https://doi.org/10.1007/s12517-020-5186-2, 2020.

Wang, C., Li, S., Lai, Y., Chen, Q., He, X., Zhang, H., and Liu, X.: Predicting the Soil Freezing Characteristic From the Particle Size Distribution Based on Micro-Pore Space Geometry. Water Resour. Res., 58(1), e2021WR030782. https://doi.org/10.1029/2021WR030782, 2021.

Weinstein, Y., Rotem, D., Kooi, H., Yechieli, Y., Sültenfuß, J., Kiro, Y., Harlavan, Y., Feldman, M., and Christiansen, H. H.: Radium isotope fingerprinting of permafrost-applications to thawing and intra-permafrost processes. Permafr. Periglac. Process, 30(2), 104-112. https://doi.org/10.1002/ppp.1999, 2019.

Weinstein, Y., Friedheim, O., Odintsov, L., Harlavan, Y., Nuriel, P., Lazar, B., Burg, A.: Using radium isotopes to constrain the age of saline groundwater, implications to seawater intrusion in aquifers. J. Hydrol., 598, 126412. https://doi.org/10.1016/j.jhydrol.2021.126412, 2021.

Wojtasik, B., Świrydowicz, S., Burska, D., and Nowiński, K.: Radionuclide activities in sediments on the northern coast of Spitsbergen. Polish Polar Research, 291-312. DOI: 10.1515/popore-2017-0019, 2017.

Yamaguchi, A., Nagata, K., Kobayashi, K., et al.: Extended X-ray absorption fine structure spectroscopy measurements and ab initio molecular dynamics simulations reveal the hydration structure of the radium(II) ion. iScience 25, 104763. https://doi.org/10.1016/j.isci.2022.104763, 2022.

Yershov, E.D.: General Geocryology. English ed. Cambridge, UK: Cambridge University Press, 1998.

Zhang, M., Zhang, X., Lu, J., Pei, W., and Wang, C. 2018. Analysis of volumetric unfrozen water contents in freezing soils. Exp. Heat Transf., 32(5), 426–438. https://doi.org/10.1080/08916152.2018.1535528, 1998.